Universidad de Concepción

Departamento de Astronomía
Facultad de Ciencias Físicas y Matemáticas

Velocity structure of the Orion A Integral Shaped Filament

(La estructura de la velocidad del filamento Integral Shaped Filament de Orión A)

Tesis para ser presentada en la dirección de postgrado de la Universidad de Concepción para optar al grado de

Magister en ciencias con mención en física

Valentina Isabel González Lobos

Asesor: Prof. Amelia Stutz

Concepción, Chile
Junio 2019

Agradecimientos

Quiero agradecer todes quienes que me apoyaron durante todo este periodo. A quienes lo hicieron desde el comienzo y a quienes llegaron durante el camino. A mis amigues y compañeres que hicieron del proceso más alegre. A mi pololo y familia que me levantaron cuando lo necesité. A aquellos profesores que mostraron su apoyo y me hicieron creer más en mi misma.

Finalmente, agradezco a Dominik Schleicher, al programa Basal y a CONICYT por el apoyo económico.

Resumen

El proceso de formación estelar es fundamental para comprender la formación de planetas y la evolución de galaxias. Casi todas las estrellas se forman en cúmulos estelares que son contenidos en filamentos masivos. Aquí presentamos un análisis de la cinemática del gas del filamento Integral Shaped Filament en Orión A utilizando observaciones de distintas transiciones moleculares (^{12}CO, ^{13}CO, NH_3, N_2H^+) para rastrear el gas a distintas densidades. Describimos la estructura de la velocidad a lo largo del filamento a través de diagramas de posición-velocidad ponderado por la intensidad o lo comparamos con la distribución de la masa del gas y las estrellas. Encontramos una gradiente de velocidad en la dirección Norte-Sur, que termina con un máximo azul en la velocidad en todas las transiciones con velocidad $\sim 7\,\mathrm{km\,s^{-1}}$ en las cercanias del centro del cúmulo Orion Nebula Cluster. Se ha popuesto anteriormente que el punto máximo azul es posiblemente originado por el colapso gravitacional del cúmulo o por la naturaleza oscilante del filamento. Sin embargo, encontramos que el máximo está desplazado con respecto al máximo en la distribución de masa y la posición del cúmulo, indicando que la acción de otras fuerzas aparte de la gravedad, como los campos magnéticos, pueden impactar la estructura observada. Caracterizamos la cinemática global del filamento a través del máximo de la velocidad de cada transición. Encontramos que en la región norte del filamento los máximos concuerdan dentro de $\sim 0.5\,\mathrm{km\,s^{-1}}$, pero observamos desviaciones significativas en la región del cúmulo. Mostramos que cerca del centro del cúmulo, las velocidades dependen de la transición. Describimos el ancho de las líneas a través de perfiles radiales de dispersión de velocidad, los que siguen el centro del filamento. Encontramos que la dispersión de velocidad no térmica depende de la transición, es decir, los trazadores más densos (NH_3, N_2H^+) son cinemticamente mas fros que los menos densos (^{12}CO, ^{13}CO). Calculamos los perfiles radiales de la energía cinética específica a partir de las dispersiónes y comparamos con el potencial gravitacional del filamento y del cúmulo. Encontramos que la nube esta unida gravitacionalmente ya que las velocidades son insuficientes para superar el potencial gravitacional. Esto implica que la nube está experimentando el colapso gravitacional o que otras fuerzas, como el campo magnético y la rotación, se requieren para reproducir la eficiencia de la formación estelar observada. Presentamos, por primera vez, la presencia de dos componentes de velocidad en el diagrama de posición-velocidad de ^{12}CO, indicando que el filamento está rotando con una velocidad angular de $\omega = 1.4\,\mathrm{Myr^{-1}}$. La es-

tructura de la velocidad observada con ^{12}CO presenta fluctuaciones en la velocidad en la forma de 6 peaks de velocidad con separaciones regulares (espacios proyectados en δ de $\sim 0.44\,\mathrm{pc}$). Al comparar las posiciones de estos peaks con objetos estelares jóvenes y catálogos de protoestrellas, encontramos que 3/6 peaks no pueden ser descartados por outflows, mientras que los otros 3 se ven no asociados con fuentes (proto)estelares conocidas. La separación de estos peaks tiene una escala temporal típica de $\sim 1\,\mathrm{Myr}$. Nuestro análisis indica que el escenario de formación de cúmulos es más complejo de lo que se pensaba. Proponemos que la acción de campos magnéticos puede impactar las características cinemáticas del filamento, Esta hipótesis puede probarse con observaciones del campo magnético y simulaciones de formación de cúmulos estelares.

Abstract

The process of star formation is fundamental to understand planet formation and galaxy evolution. Almost all stars form in clusters embedded in massive filaments. We present an analysis of the gas kinematics of the Integral Shaped Filament in Orion A using different molecular transitions (^{12}CO, ^{13}CO, NH_3, N_2H^+) to trace different gas densities. We describe the velocity structure along the filament with intensity-weighted position-velocity diagrams and compare it with the mass distribution of stars and gas. We find a North to South velocity gradient that terminates with a blue-shifted velocity peak seen in all tracers at $\sim 7\,\mathrm{km\,s^{-1}}$, close to the center of the Orion Nebula Cluster (ONC). The blue peak has been previously proposed to originate to originate either from the gravitational collapse of the ONC or the wave-like nature of the gas filament. We find that this blue peak appears offset form the peak of the mass distribution and position of the ONC, suggesting that the action of forces other than gravity, such as magnetic fields, shape the observed velocity structure and wave-like structure. We characterize the global kinematics of the filament with velocity ridgelines of each tracer. We find that in the northern portion of the filament the ridgelines agree within $\sim 0.5\,\mathrm{km\,s^{-1}}$, but observe significant deviations in the cluster region. We show that near the center of the cluster, the gas velocities depend on the molecular tracer. We describe the linewidths of the four tracers with velocity dispersion radial profiles, following the center of the filament. We find that the non-thermal velocity dispersions strongly depend on the tracer, that is, the higher density gas (NH_3, N_2H^+) is kinematically colder than the lower density gas (^{12}CO, ^{13}CO). We compute the specific kinetic energy profile from the linewidths and compare with the gravitational potential profiles of the filament and cluster. We find that the cloud is gravitationally bound as velocities are insufficient to surpass the gravitational potential. This implies that either the cloud is undergoing gravitational collapse or that other forces, such as magnetic fields and rotation, are required to reproduce observed star formation efficiencies. We report, for the first time, the presence of two velocity components present in the full ^{12}CO position-velocity diagram, suggesting that the filament is rotating with an angular velocity of $\omega = 1.4\,\mathrm{Myr^{-1}}$. The velocity structure of ^{12}CO presents velocity fluctuations in the form of 6 velocity peaks with regular separations ($\sim 0.44\,\mathrm{pc}$ spacing in projection in δ). Comparison of these peaks positions to young stellar objects and protostar catalogs reveals that 3/6 peaks cannot be ruled out by outflows, while the other 3 appear

unasocciated to known (proto)stellar sources. The separation of the peaks has a characteristic timescale of $\sim 1\,\mathrm{Myr}$. Our analysis suggests that the cluster formation scenario is more complex than previously thought. We suggest that the action of magnetic fields impacts the kinematic features of the filament. This hypothesis can be tested with magnetic field observations and cluster formation simulations.

Contents

List of Figures

Chapter 1

Introduction

The Orion A molecular cloud has been a common target for star formation studies, because it is nearby and hosts a rich young cluster with ongoing massive star formation. The process of star formation occurs in a cold and dense medium inside molecular clouds, it involves gravity, turbulence, magnetic fields and stellar feedback. The physical models that explain how massive stars form have remained controversial because of the difficulties involved in studying young clusters embedded in molecular gas, such as dust obscuration, resolving individual objects at large distances and producing models and simulations of a process with complicated physics.

Cold molecular gas is directly associated with star formation, being the material from which stars form. Observations of the line emission of different molecular transitions make it possible for us to study the physical conditions of the cold gas in the insterstellar medium. Line emission observations provide us information about the mass, temperature and kinematics of the molecular gas. Learning the physical conditions of the cold gas allows us to better understand the underlying physical process of star formation.

Our work focuses on the gas kinematics of a massive star forming molecular filament in the Orion A molecular cloud, the Integral Shaped Filament (ISF) (Bally et al., 1987). We aim to study the gas kinematics through radial velocity observations of the line emission from the gas at different densities, in order to understand the role of the physical mechanisms taking place during the formation of stars.

We used public observations of the ISF of different molecular transitions: ^{12}CO, ^{13}CO, NH_3 and N_2H^+. These transitions trace different density regimes of the molecular gas. The observations are stored as spectral cubes, three dimensional data with two spatial and one spectral coordinates. The spectral axis is a representation of the Doppler shift in frequency caused by the line of sight movement of the gas. This allows us to extract kinematic information at each position through the observed region, including velocity integrated emission, central velocity of the line and velocity dispersion.

These parameters were used to construct intensity-weighted position-velocity diagrams, ve-

locity ridgelines and velocity dispersion radial profiles of the filament, which give us an idea of the velocity structure (at global and smaller scales) and turbulent energy of the filament respectively. The velocity structure of the ISF was compared with the mass distribution of the gas and stars and the protostars positions in order to find evidence for gravitational collapse and stellar feedback. The velocity dispersion radial profiles were used to quantify the turbulent energy and then compare with the gravitational potential energy. These comparisons represent a test for the relative importance of the different physical mechanisms mentioned.

This thesis is organized as follows. Chapter 2 includes an introduction to the topic of star formation including observations and theory, focusing on the process of massive star formation in young embedded clusters and the ISF region. Chapter 3 introduces the concept of spectral cubes and presents the datasets used in this project. Chapter 4 adresses the analysis tools used to extract the kinematic information from the datasets. Chapter 5 presents the main results from the kinematic analysis. Chapter 6 is a summary and discussion of the results along with the conclusions of this work.

Chapter 2

Star Formation

2.1 Key concepts: Initial Mass Function and the Star Formation Law

Our work develops in the context of star formation. The process of star formation is fundamental to understand galaxy evolution and planet formation. The lifetime evolution of a star is determined by its mass, this is ultimately established by the physical conditions and processes taking place during its formation.

The formation of stars produces a distribution of different stellar initial masses that can be described using the Initial Mass Function (IMF). The IMF is the number of stars as a function of mass, it is typically represented using a power law of the form

$$\Phi(\log m) = \frac{dN}{d\log m} \propto m^{-\Gamma}, \tag{2.1}$$

where m is the mass of a star, N is the number of stars in a logarithmic mass range (Bastian et al., 2010). This form of the IMF was first introduced by Salpeter (1955) with an index of $\Gamma \sim 1.35$. Follow-up studies suggest that the IMF is roughly universal and is fit with a lognormal distribution (broken power law) with a broad peak from 0.1 to 0.6 $M_\odot$ (Bastian et al., 2010; Krumholz, 2015; Lada and Lada, 2003).

Figure 2.1 shows the present day mass function of young star forming regions, open clusters, globular clusters and the inferred field star IMF from Bastian et al. (2010). The plot shows that the same IMF appears universally, when taking into account the shift towards greater characteristic mass in globular clusters due to dynamical evolution (Bastian et al., 2010). The peak of the IMF represents the typical mass produced by the star formation process, which is between $0.1 - 0.6\,M_\odot$ (Lada and Lada, 2003).

We see from the IMF that the process of star formation produces few high mass stars compared to lower mass stars, but massive stars release a great amount of energy into a galaxy because of their radiation, winds and supernova explosions (Motte et al., 2017).

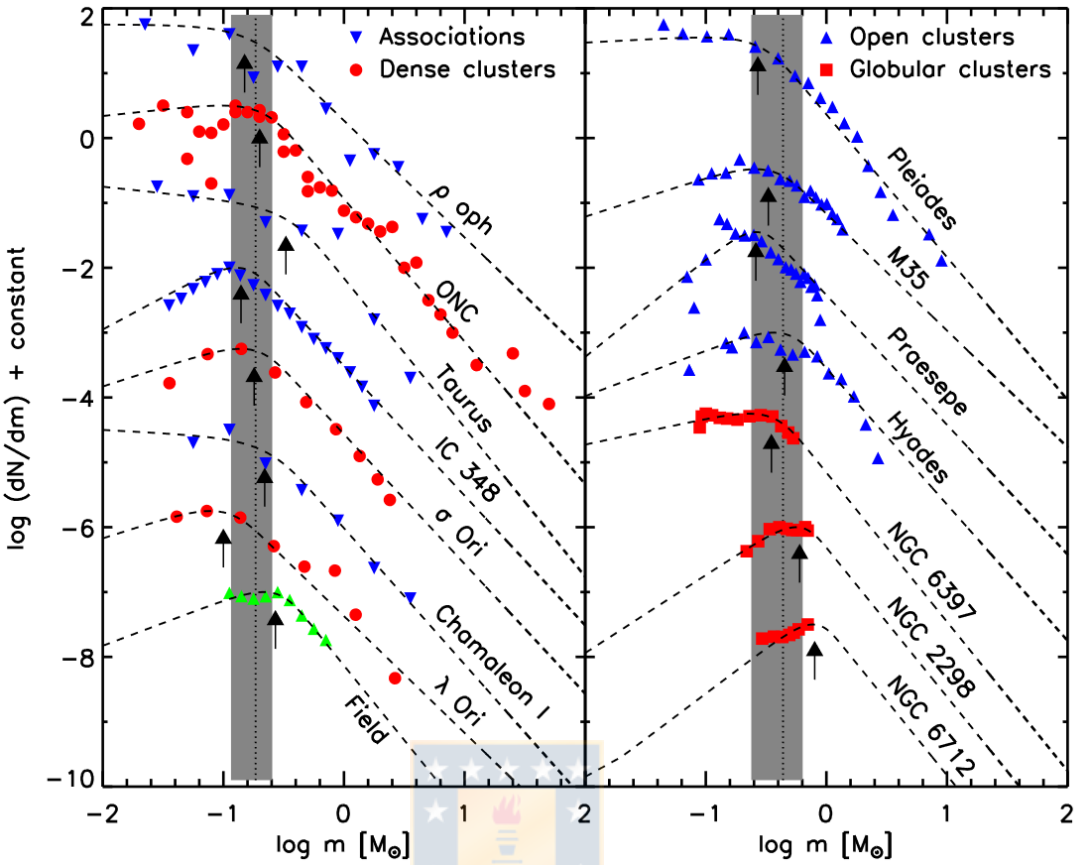

Figure 2.1: Plot from Bastian et al. (2010) of the derived present day mass function of a sample of young star-forming regions, open clusters of all ages, old globular clusters and the inferred field star IMF. The dashed line represents the power law fits of the 'tapered power-law' IMF from De Marchi et al. (2005). Arrows indicate the characteristic mass of each fit, the dotted line represents the mean characteristic mass of each panel with its corresponding standard deviation shaded in grey.

Star formation occurs in cold and dense regions called molecular clouds, which are distributed in the spiral arms of galaxies. Observations show that there is a linear correlation between neutral gas and star formation when averaging over galactic scales (Kennicutt, 1998). The idea was first introduced by Schmidt (1959) as a scaling relationship between the gas surface density (gas mass per unit area) and star formation surface density (star formation rate per unit area). Figure 2.2 shows the relationship between the disk-averaged star formation surface densitites as a function of the gas surface densitites for different star-forming galaxies from Kennicutt and Evans (2012). The plot shows that the different galaxies tightly follow the star formation relationship with a power-law index of $N = 1.4$ introduced in (Kennicutt, 1998).

A useful parameter that arises from this relationship is the depletion time, which is the time required to turn all gas into stars. The depletion time corresponds to the ratio between the

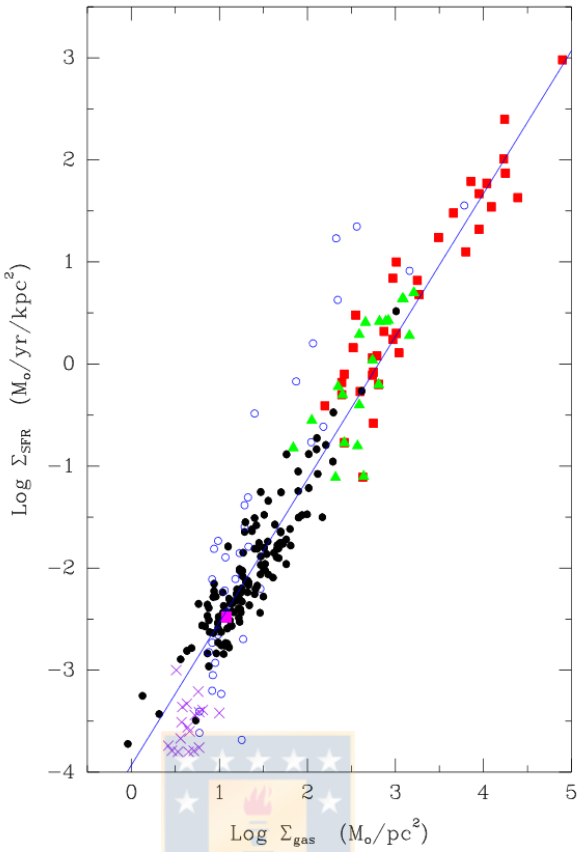

Figure 2.2: Plot of the disk-averaged star formation surface densitites as a function of the gas surface densities for different classes of star-forming galaxies from Kennicutt and Evans (2012). Each point is a galaxy, black points are normal galaxies, blue open circles are metal poor galaxies, purple crosses are measurements from low surface brightness galaxies, green triangles are measurements from the centers of the normal disk galaxies and red squares are starburst galaxies. The line represents a power-law with index of $N = 1.4$ from Kennicutt (1998).

molecular gas mass and the star formation rate

$$t_{\rm dep} = \frac{M_{\rm gas}}{\dot{M}_*}, \tag{2.2}$$

where $\dot{M}_*$ corresponds to the rate of stars being formed in units of $[\mathrm{M}_\odot\,\mathrm{yr}^{-1}]$ (Krumholz, 2015).

The depletion time in our Galaxy is about $t_{\rm dep} \sim 1\,\mathrm{Gyr}$ (Krumholz, 2015), this is around two orders of magnitude greater than the free-fall time. The free-fall is the time needed for a mass distribution to collapse by its own gravity, in the case of an isothermal sphere it is given by

$$t_{\rm ff} = \sqrt{\frac{3\pi}{32G\rho}}, \tag{2.3}$$

where ρ is the density of the sphere and G is the gravitational constant (Krumholz, 2015). The much larger timescale of the depletion time suggests that star formation is a very inefficient

process (at galactic and molecular cloud scale) and only a fraction of the total gas in a galaxy is converted into stars (Evans, 1999; Robitaille and Whitney, 2010; Krumholz, 2015).

2.2 Observational techniques in star formation

The formation of a star begins with the gravitational collapse of a cold and dense core, during this time the protostar is fully embedded in molecular gas and dust that obscures the process in optical and UV wavelengths. In order to study the early phases of star formation we must trace the dust and cold gas, requiring infrared and sub-mm observations (van Dishoeck, 2004).

Thermal dust emission is determined by the Planck function and the opacity of the medium and it is detected in far infrared wavelengths. Also, dust absorption of the stellar background is detected in near infrared wavelengths (van Dishoeck, 2004; Krumholz, 2015). Figure 2.3 shows an RGB composite of the central region of the Carina Nebula from *Herschel* observations at $70\,\mu$m, $160\,\mu$m and $350\,\mu$m (Preibisch et al., 2012). The Carina Nebula is one of the most massive star forming regions in the Galaxy and presents a high amount of stellar feedback from massive stars, the figure shows the cloud's filamentary structure dominated by stellar feedback (Preibisch et al., 2012).

Gas is traced by molecular line emission. Molecular line profiles contain information about the velocity produced by motions along the line of sight. Maps of the line center velocity and linewidth can provide a view of the overall kinematics of the gas. The most common tracers are the rotational lines of CO, because CO is the most abundant molecule in the cold ISM after H_2 and is conveniently found in the same places. CO is generally used to infer the gas mass of a cloud (Evans, 1999; Krumholz, 2015). Other common molecular tracers are formed from the most abundant atoms in the universe H, He, O, C and N, these include but not limited to HCN, N_2H^+, ^{13}CO, NH_3. Figure 2.4 shows a composite of the ^{12}CO (2-1) ALMA integrated emission (orange) and Hubble (blue) observations of the M74 spiral galaxy, as part of the PHANGS-ALMA survey (Sun et al. 2018; Leroy et al. in prep.). The figure shows the spatial correlation between molecular gas and star formation (traced by the light from young massive stars).

Molecular line emission is highly dependant of the physical conditions in the gas, there must be equilibrium between energy levels for the transition to be detected. The excitation and de-excitation balance of energy levels can be simplified considering a population of molecules with two energy levels and their rates of spontaneous emission and collisions. The spontaneous emission from a *upper* to a *lower* level is represented by the Einstein coefficient A_{ul} in units of $[s^{-1}]$. Collisions are represented by the collisional coeficient k_{ul} in units of $[cm^3\,s^{-1}]$.

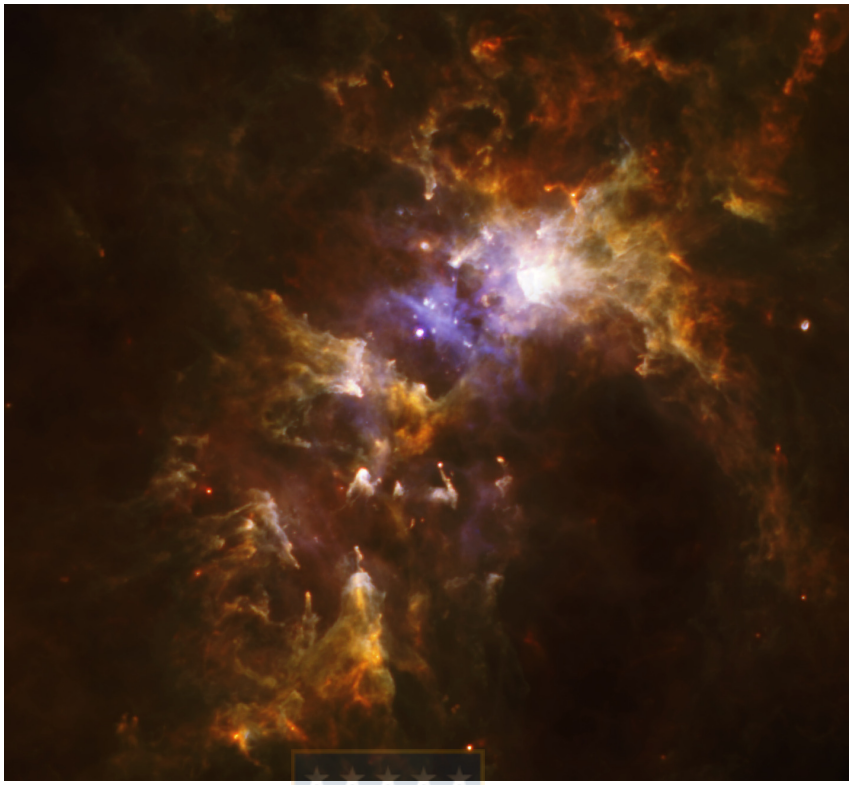

Figure 2.3: RGB composite of the central region of the Carina Nebula Complex, constructed from *Herschel* observations at 70 μm in blue, 160 μm in green and 350 μm in red (Preibisch et al., 2012). The colors trace different dust temperatures (considering the peak of the Planck emission at each wavelength), the 70 μm band traces temperatures of $T \sim 72\,K$, the 160 μm band traces $T \sim 32\,K$ and the 350 μm band traces $T \sim 15\,K$ (Preibisch et al., 2012).

The critical density is defined as the ratio between A_{ul} and k_{ul}:

$$n_{\text{crit}} = \frac{A_{ul}}{k_{ul}}. \tag{2.4}$$

The critical density is the density at which a transition is excited and produces radiation at sub-mm wavelengths (Shirley, 2015). Therefore, different transitions give us information of different density regimes in the gas.

2.3 Physical conditions in star forming regions

Although star formation seems to be a universal process at large scales (see Section 2.1), observations show that there is a broad range of morphologies and physical conditions between star forming regions. For example, the Bok Globule Barnard 68 has a size of 0.2 pc and a mass of 3 $M_\odot$, it is a dense starless core (Alves et al., 2001). The B211 filament in the Taurus cloud has a mass per unit length of 54 $M_\odot$ pc^{-1} and is forming low mass, dispersed stars (Palmeirim et al.,

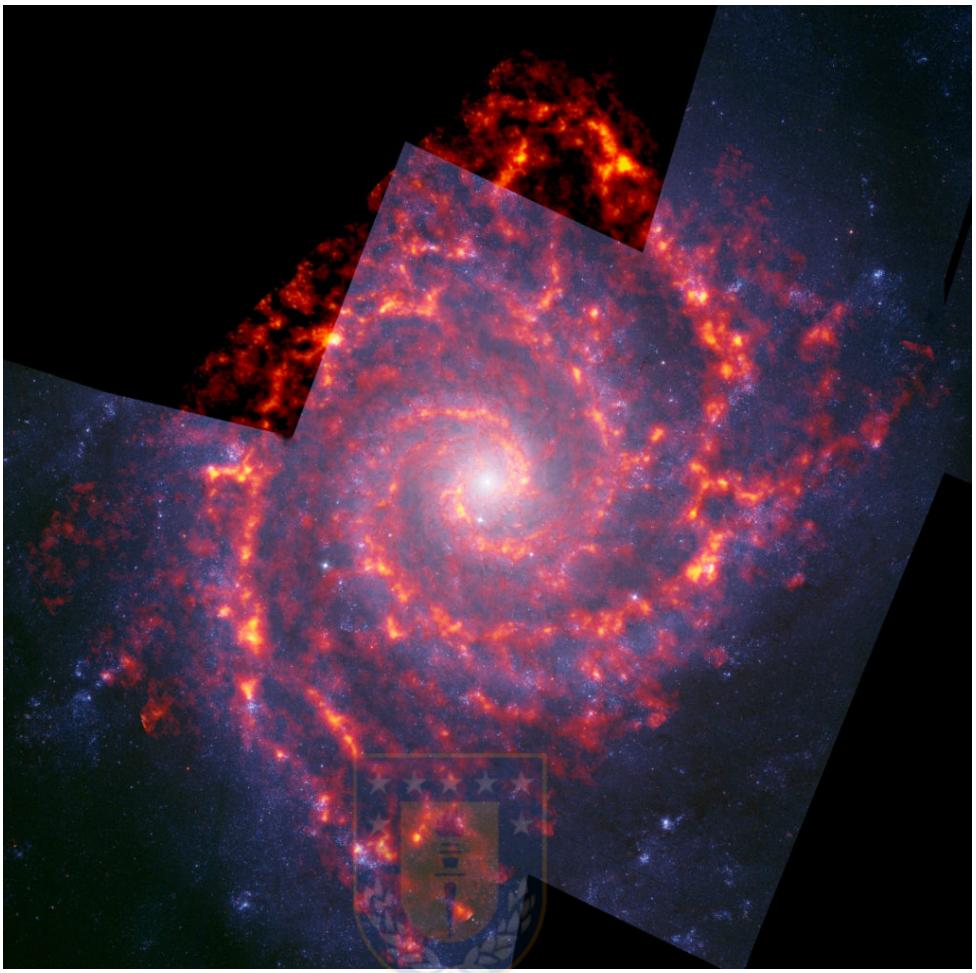

Figure 2.4: Composite of ^{12}CO (2-1) ALMA (orange) and Hubble (blue, from the Hubble Legacy Archive) observations of M74, as part of the PHANGS-ALMA survey to study the properties of the star-forming molecular clouds in nearby spiral galaxies (Sun et al. 2018; Leroy et al. in prep.). Credit: NRAO/AUI/NSF, B. Saxton: ALMA (ESO/NAOJ/NRAO); NASA/Hubble[1].

2013). These two regions are examples of low mass isolated star formation.

On the other hand, the Integral Shaped Filament (Bally et al., 1987) in Orion A is a massive filament with a length of $\sim 7\,\mathrm{pc}$ and a line mass of $\sim 400\,\mathrm{M}_\odot\,\mathrm{pc}$ (Kainulainen et al., 2017) and is forming a cluster of stars, called the Orion Nebula Cluster, in the densest regions along the filament (Stutz and Gould, 2016; Kainulainen et al., 2017). This embedded young cluster is forming thousands of stars and has already formed the massive OB stars from the Trapezium cluster (Lada and Lada, 2003).

Observations provide us information about the physical conditions in star forming regions. Molecular clouds are cold and dense regions of the insterstellar medium (ISM), they occupy

[1]https://sites.google.com/view/phangs/gallery

a small fraction of the ISM but contain a significant fraction of its mass (McKee and Ostriker, 2007). Molecular clouds have sizes of tens of pc and characteristic surface densities of $\sim 100\,M_\odot\,pc^{-2}$ (Krumholz, 2015), they are organized in a hierarchical fractal-like structure (McKee and Ostriker, 2007; Krumholz, 2015) where most of the gas is in a relative lower density phase and a little is in dense regions, resulting in a clumpy distribution of gas across the cloud.

Not only the structure of clouds is complex, but also their velocities are complicated. Molecular line observations of the dense gas show that the velocity spreads are larger than the spread caused by thermal broadening (Evans, 1999). Moreover, molecular clouds obey a linewidth-size relationship where velocity dispersions increase as a power of the size and are supersonically tubulent (Larson, 1981; McKee and Ostriker, 2007; Krumholz, 2015).

Molecular clouds have also been observed to be highly magnetized. Zeeman effect and dust polarization observations allow us to infer the strength and direction of the magnetic field from the ISM. Magnetic fields play a very important role in the regulation of star formation, they dominate turbulent flows that control the formation of clouds and cores that could eventually become self-gravitating allowing the formation of stars (Crutcher, 2012).

When a molecule is in the presence of a magnetic field, the Zeeman effect causes the emitted line to split into two components shifted in frequency. The Zeeman effect is used to measure the strength and direction of the line of sight magnetic field (Crutcher, 2012). Zeeman splitting observations of molecular clouds have revealed that internal supersonic motions are likely to arise from magnetohydrodynamics (MHD) and that magnetic fields play an important role in molecular clouds, but they are unable to support clouds against gravity (Crutcher, 1999).

Dust polarization is detected in regions with dust emission and absorption. Polarized starlight is a probe of the plane of the sky magnetic field morphology in the ISM. The effect of polarization requires the alignment of dust grains. Alignment occurs when radiation external to the clouds or polarized protostellar light is differentially scattered by dust grains. The process of scattering spins the grains aligning their extinction cross section perpendicular to the magnetic field (Crutcher, 2012). Dust polarization observations have revealed that magnetic field morphologies in the ISM are ordered, smooth and in correlation with the galactic plane, suggesting that the magnetic field is strong enough to resist twisting by turbulence (Crutcher, 2012). Magnetic field morphologies of some dense cores reveal a hourglass structure that would arise from gravitational contraction along the field lines, suggesting that magnetic fields play a critical role in the collapse of the gas and the formation of stars (Crutcher, 2012). Figure 2.5 shows the magnetic field direction inferred from polarization observations of the Orion Molecular Cloud at optical and sub-mm wavelengths (Li et al., 2009). The figure shows that spatially separated cores have similar field directions, which in addition are close to the mean field direction

of the inter-cloud medium (Li et al., 2009).

2.4 Physics of star formation

As mentioned in section 2.1 star formation is a very inefficient process, where only a fraction of all the gas available in molecular clouds is transformed into stars (Robitaille and Whitney, 2010). The fraction of molecular gas transformed into stars ($\Sigma_{\rm SFR}/\Sigma_{\rm gas}$ in units of $\rm yr^{-1}$) is called the star formation efficiency (SFE), the observed SFE is low and ranges from 10%-30% (Lada and Lada, 2003). The SFE is the inverse of the depletion time (see Equation 2.2) This suggests that other physical processes must provide clouds with support against gravitational collapse.

The main physical processes involved in star formation are gravity, turbulence, magnetic fields and feedback from protostars or nearby massive stars (McKee and Ostriker, 2007, see also Kroupa et al., 2018 on feedback in Orion). Turbulence, magnetic fields and protstellar jets can act together as a physical mechanism against gravitational collapse (Federrath and Klessen, 2012; Federrath, 2016).

Cloud mass is the parameter that determines the gravitational potential and it is fundamental to determine cloud evolution. Clouds undergo gravitational instabilities that cause fragmentation, collapse will occur in fragments (clumps/cores) that exceed the Jeans mass. A cloud with only thermal support will collapse in a free-fall time (equation 2.3), this is not the observed case so other forces must act as a support mechanism (Evans, 1999; Lada and Lada, 2003; Krumholz, 2015).

As it was mentioned in Section 2.3, molecular clouds follow a linewidth-size relationship arising from supersonic internal motions. This relationship indicates that turbulent energy decays into smaller regions via the formation of shocks. The density distribution of the gas in a cloud is shaped by strong converging shocks that generate overdense regions, these can eventually become self-gravitating (and allow gravitational instabilities and collapse to take place) (Lada and Lada, 2003; Krumholz, 2015). The effects of turbulence on global scales are well understood, but the source of turbulence is unknown.

Magnetic fields in the ISM are characterized by flux freezing, which means that the magnetic field lines are frozen into the ionized fluid and both move together (Krumholz, 2015). Most molecular clouds have comparable turbulent and magnetic energies. However, the mass to magnetic flux ratio indicates that molecular clouds are supercritical, implying that magnetic fields only are not strong enough to provide pressure against gravitational collapse (Crutcher, 2012).

MHD simulations of a low mass molecular cloud including different physical models: gravity only, gravity vs. turbulence, gravity vs. turbulence + magnetic fields and gravity vs. turbulence + magnetic fields + stellar feedback; it was found that the time needed to reach a SFE of 20% in

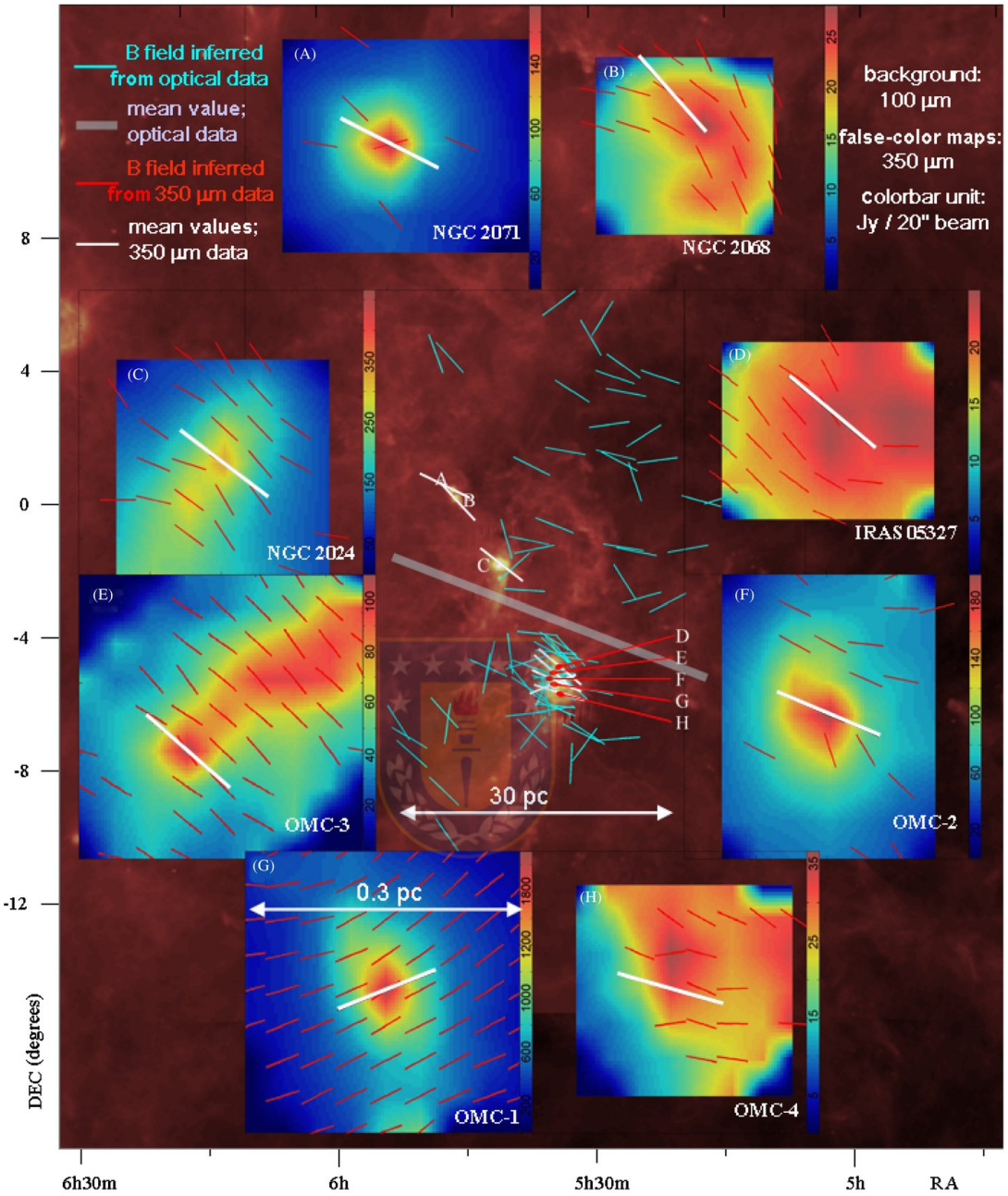

Figure 2.5: Magnetic fields in the Orion Molecular Cloud from Li et al. (2009). The background is the IRAS 100 μm map. The magnetic field directions inferred from optical data (shown with blue vectors) and mean of the optical data (shown with a gray vector) are superimposed. The insets, labeled A through H, show polarimetry observations carried out with the Caltech Submillimeter Observatory at 350 μm of eight cores in the cloud, the polarimetry is shown as color intensity maps, the direction of the polarization is shown with red vectors and the mean direction of the polarization is shown with white vectors (Li et al., 2009).

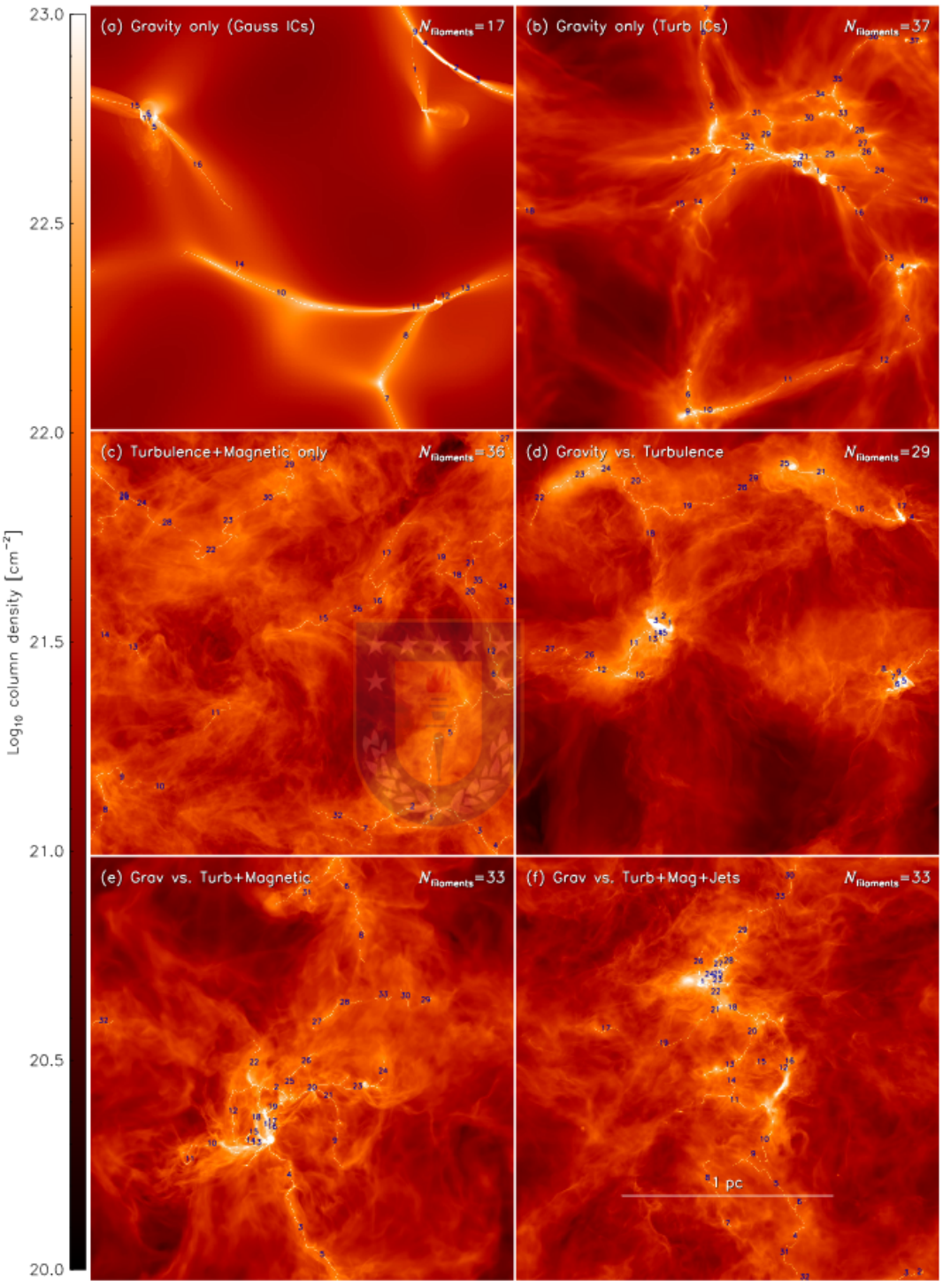

Figure 2.6: Column density projections from simulations with different physical models: (a) Gravity only from Gaussian initial conditions, (b) Gravity only from turbulent initial conditions, (c) MHD turbulence, (d) Gravity vs. Turbulence, (e) Gravity vs. Turbulence + Magnetic fields and (f) Gravity vs. Turbulence + Magnetic Fields + Outflow Feedback (Federrath, 2016).

the cluster formed varied with the models. The SFE decreased with the addition of forces other than gravity. The model with gravity, turbulence, magnetic fields and feedback produced SFR consistent with observations (Federrath, 2016). Figure 2.6 shows the column density projections of the simulations from Federrath (2016). We can see that networks of filaments are produced in all models. The presence of feedback and magnetic fields affects the number and distribution of the filaments but not their characteristic properties, such as the filament width (which appears to be universal with a value of 0.1 pc) (Federrath, 2016).

Feedback processes include: bipolar outflows of material being carried away from protostellar accretion disks, radiation pressure caused by the photons of newborn stars, ionizing radiation from massive stars, shocks from fast winds of massive stars and when stars with masses $> 8\,M_{\odot}$ explode as supernova (Krumholz et al., 2014). Stellar feedback impacts the ISM and is a candidate in reducing the SFE (Krumholz, 2015). Feedback is much more important in regions of massive star formation, because the high energy output of massive protostars (and following massive stars) is injected directly into the ISM. Multiple young massive stars could even disrupt their entire parent cloud (Lada and Lada, 2003; Zinnecker and Yorke, 2007; Krumholz, 2015). Stellar feedback can also trigger new star formation, because it provides external pressure that can compress molecular cloud layers and facilitate the formation of gravitational instabilities (Zinnecker and Yorke, 2007).

The current star formation paradigm estates that large scale supersonic motions govern the macrophysics of star formation (McKee and Ostriker, 2007). The hierarchical structure seen in the ISM would be a result of its turbulent nature, allowing the formation of structure in molecular clouds that ultimately leads to star formation (Lada and Lada, 2003). A combination of the processes mentioned above participate in the regulation of star formation where supersonic turblence, magnetic fields and stellar feedback act together as a mechanism against gravitational collapse, reducing the large scale SFE. Once gravitational collapse starts the envelope is slowly decoupled from the turbulent flow and local magnetic field (Lada and Lada, 2003).

2.5 Massive star and cluster formation

We have mentioned the effect of massive stars on their environment. Massive stars produce a great amount of energy in all stages of their evolution: during their formation, during their time in the main sequence and when they explode as supernova. We expect that they greatly impact their birthsites during and after their formation. Figure 2.7 shows the color composite of the DR21 ridge in Cygnus X observed with the SPIRE and PACS instruments of *Herschel*. The DR21 is the densest and most massive structure in the Cygnus X region located at 1.4 kpc, it is host to an HII region and massive protostars and presents evidence of mass flows through connected filaments into the ridge (Hennemann et al., 2012). The DR21 ridge hosts 22 dense

cores (with some massive) and represents a probable region to host the most massive forming star cluster in Cygnus X (Hennemann et al., 2012).

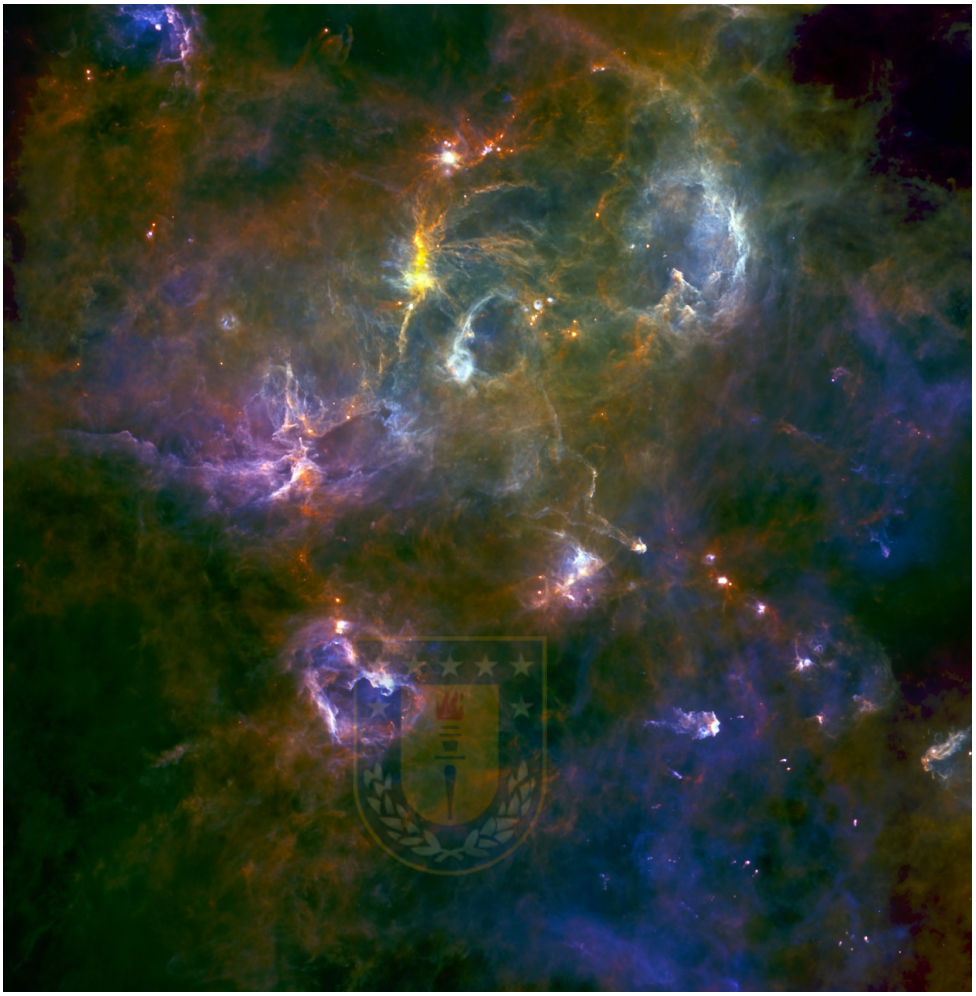

Figure 2.7: Color composite of *Herschel* ofbservations at 250 μm with the SPIRE instrument (red), 160 μm with the PACS instrument (green) and 70 μm with PACS (blue) of the DR21 ridge in Cygnus X from Hennemann et al. (2012) as part of the HOBYS key programme (Motte et al., 2010). We see the filamentary structure of the cloud that converges at the ridge and the great impact that massive stars have on the cloud. Credits: ESA/PACS & SPIRE consortium, HOBYS key programme, Martin Hennemann & Frdrique Motte, Laboratoire AIM Paris-Saclay, CEA/Irfu - CNRS/INSU - Univ. Paris Diderot, France[2].

Massive stars form exclusively in clusters embedded in massive molecular filaments. Young embedded clusters are also the birthsite of almost all stars ($70\% - 90\%$) (Lada and Lada, 2003). Studying the process of massive star formation in young clusters allow us to understand the process that forms almost all stars and ultimately produces the stellar IMF. The effects of turbulence, magnetic fields and stellar feedback are important in these regions (Lada and Lada, 2003). The physical conditions and mechanisms introduced in Sections 2.3 and 2.4 are present

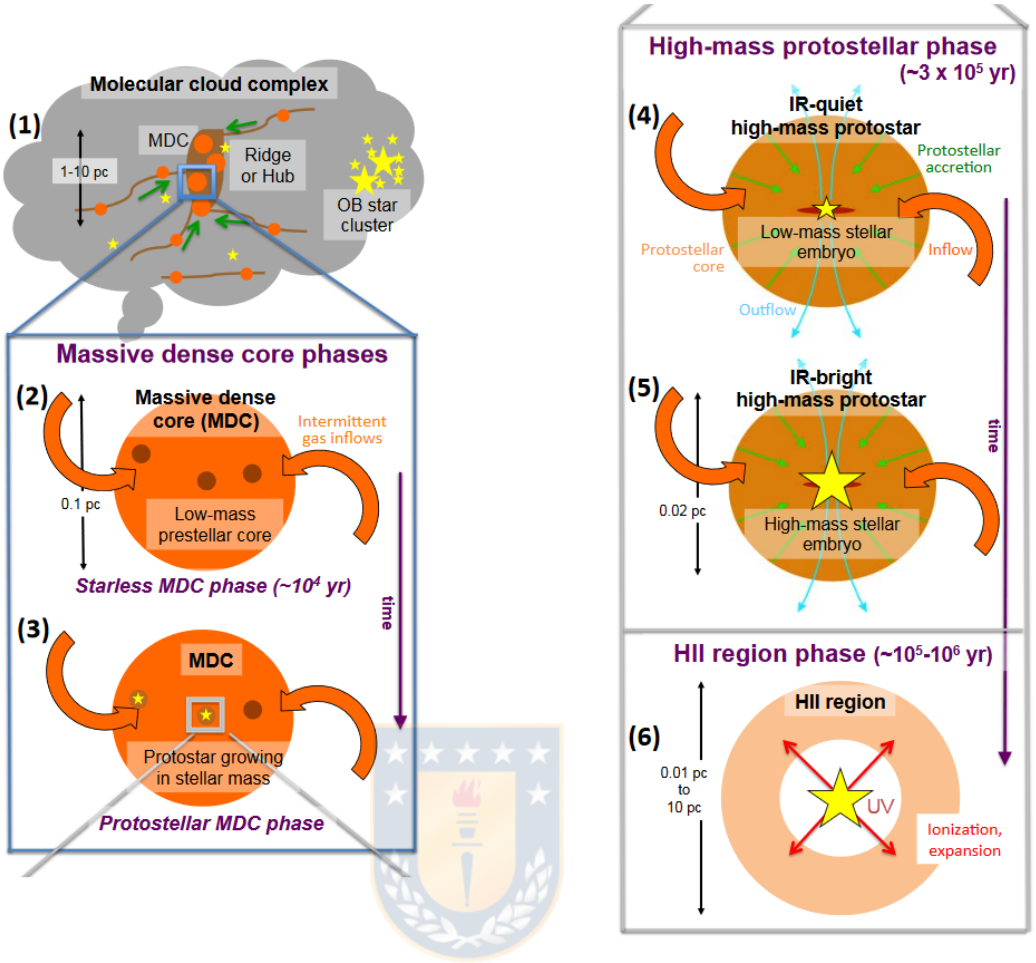

Figure 2.8: Massive star formation evolutionary scenario proposed in Motte et al. (2017). The diagram represents the different stages of massive star formation their respective spatial scale and duration .

in regions of massive star and cluster formation and determine their evolution.

Massive star formation is difficult to study because of observational and computational limitations. These include the iability to resolve individual sources as a combination of large distances and crowding in young clusters, for example, in the Orion Nebula Cluster (ONC) the stellar density in the center reaches $\sim 10^5\,\mathrm{pc}^{-3}$ (Krumholz, 2015). Also, the short timescales of the process give a small time window in which we can observe ongoing massive star formation (Motte et al., 2017). The requirements of performing detailed simulations of high mass star forming clouds are high because the physics are complex. These difficulties result in that theories of star formation remain controversial.

The process of massive star formation is highly dynamic and occurs in short timescales

[2]http://oshi.esa.int/image.html?id=88

(Motte et al., 2017). Motte et al. (2017) proposed an evolutionary scenario of high mass star formation illustrated in Figure 2.8.

The scenario considers that massive stars and clusters are formed in giant molecular clouds (GMCs), which are highly structured. GMCs are inhomogeneous and the gas is distributed in filaments with lengths of $1 - 10\,\mathrm{pc}$ (Motte et al., 2017), the stars form in these filaments and follow the dense gas distribution and kinematics (Krumholz, 2015). The gas in filaments is arranged in discrete massive dense cores with scales of $\sim 0.1\,\mathrm{pc}$ that occupy $< 10\%$ of the area of a GMC (Motte et al., 2017; Lada and Lada, 2003). However, cores represent most of the mass of a giant cloud (Lada and Lada, 2003). These cores have enhanced densities ($> 10^5\,\mathrm{cm}^{-3}$), greater linewidths and harbour the conditions to allow cluster formation (Lada and Lada, 2003; Motte et al., 2017). Massive cores further fragment into prestellar cores, a protostar formed in the center of a core will accrete gas from its envelope. Accretion occurs through gas flow streams that increase the mass of the envelope and the protostar, at this point the protostar becomes IR-quiet with strong accretion and outflows. Eventually the protostar can grow to high mass from the infalling core at $\sim 0.01\,\mathrm{pc}$ scales. When the protostar reaches more than $8\,\mathrm{M}_\odot$, the luminosity increases and the star becomes IR-bright. Soon after the star becomes luminous, it develops an HII region that slows and eventually stops accretion (Motte et al., 2017).

2.6 The Integral Shaped Filament and the Orion Nebula Cluster

The Orion Nebula is the largest nearby molecular cloud complex ($d \sim 420\,\mathrm{pc}$), the nebula is host to several associations of young stars (O'dell, 2001). One of these is an HII region associated with a young cluster that includes massive stars. This cluster is called the Orion Nebula Cluster (ONC) and it is partially embedded in a massive molecular filament called the Integral Shaped Filament (ISF) (Bally et al., 1987). The ONC contains around ~ 2000 stars spread over $\sim 4\,\mathrm{pc}$ (Lada and Lada, 2003). The ONC has ongoing high mass star formation and formed in the past the OB stars of the Trapezium cluster, which lies right in front of the ONC. The ONC might be a result of triggered star formation caused by the impact of the close HII region pushing the gas behind it (Zinnecker and Yorke, 2007). The ISF allows us to make detailed observations of massive star and cluster formation.

The ISF has a wave-like appearance (Stutz and Gould, 2016; Stutz, 2018) and presents evidence of a helical magnetic field that wraps around the filament (Heiles, 1997), this is seen from the change in field direction in opposite sides of the filament and the field direction in front of the cloud (nearly perpendicular to the filament long axis). Figure 2.9 shows the stellar polarization and Zeeman splitting observations from the Orion A molecular cloud (Heiles, 1997). Also, the magnetic field morphology seems to evolve smoothly from large to smaller scales and is usually perpendicular to the major axis on the cores within the filament, consistent with the morphology for gravitational contraction along field lines (Crutcher, 2012).

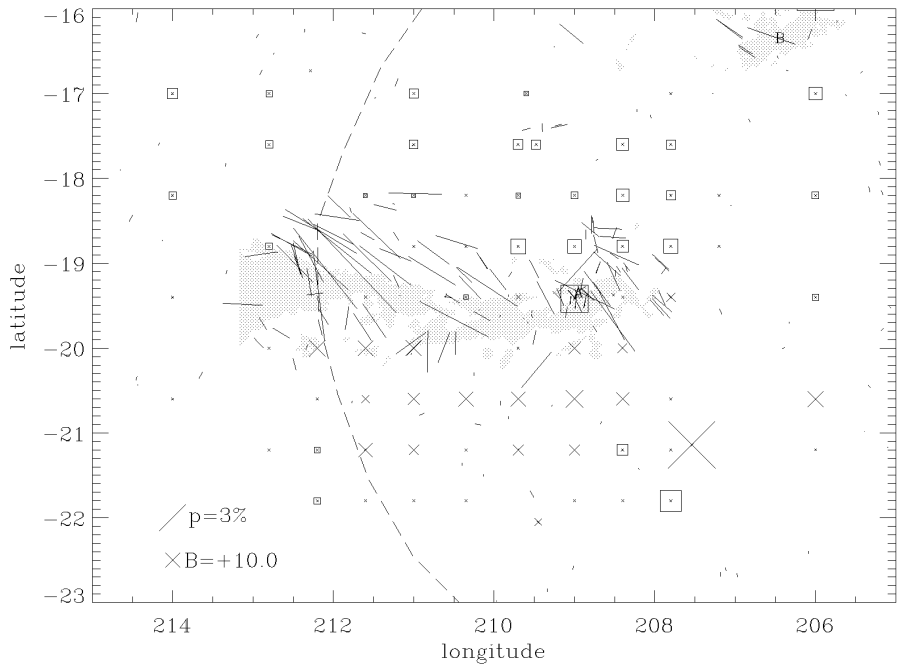

Figure 2.9: Stellar polarization (lines) and Zeeman splitting detections of the line of sight magnetic field (crosses and squares) over the Orion A region observed in ^{13}CO (stippled region) from Heiles (1997). Positive magnetic fields are represented as crosses and negative fields are represented as squares. The figure shows that the magnetic field lines are inverted in opposite sides of the filament, suggesting that the magnetic field has a helical morphology. In this Figure, the ISF is located at around longitude ~ 209.

Observations of the protostar positions on the ISF show that they lie projected on the filament and their radial velocities are consistent with those of the filament. On the other hand, more evolved young stars lie off the filament and their radial velocities differ from those of the filament by several $\mathrm{km\,s^{-1}}$ (Stutz and Gould, 2016). These observations combined with the wave-like appearance and the helical magnetic field morphology, led to propose the ejection of protostars by magnetically induced oscillations. This is a dynamical model for the ISF called the slingshot mechanism introduced in Stutz and Gould (2016). An illustration of how protostars are ejected from the ISF is presented in Figure 2.10.

The slingshot model has been tested in Boekholt et al. (2017) with numerical simulations of young stars in a cylindrical gas potential that oscillates sinusoidally perpendicular to the length of the filament. Their results show that a moving filament can reproduce the observed distribution and velocity heating of the stars (see also Matus-Carrillo et al. in prep). Figure 2.11 shows the time evolution of stars in an oscillating filament from the simulations of Boekholt et al. (2017), this shows that stars can get ejected from an oscillating filament and that this is a potential mechanism for the observed heating of stars (Boekholt et al., 2017). These simulations

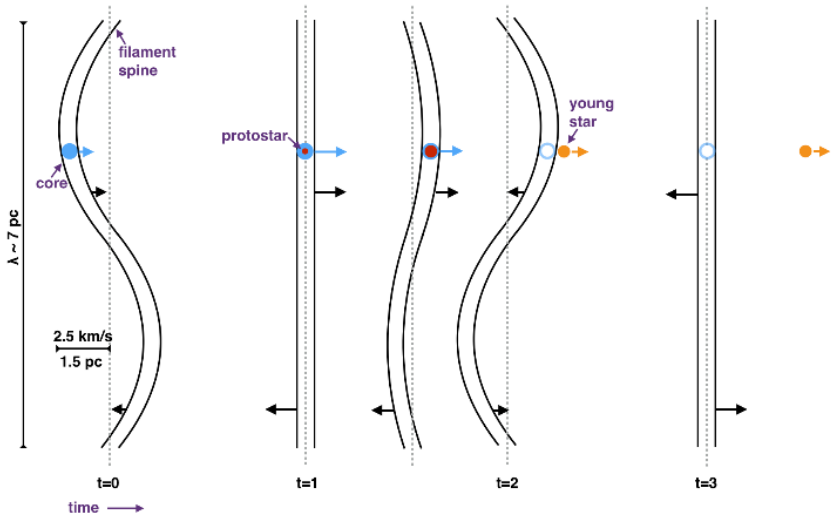

Figure 2.10: Diagram illustrating the time series of the ejection of protostars caused by the slingshot mechanism in the ISF from Stutz and Gould (2016). At $t = 0$ a protostellar core is formed in the filament, at $t = 1$ the core forms a protostar that remains embedded in the filament as it grows, at $t = 2$ the acceleration of the filament causes the protostar to decouple from the gas, at $t = 3$ the ejected young star is no longer bound to the filament.

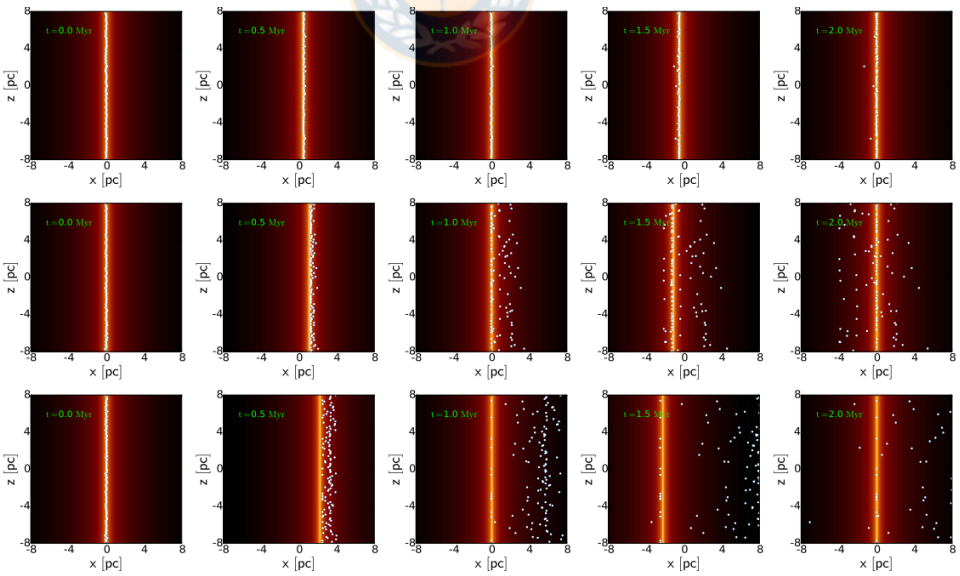

Figure 2.11: Diagram that shows the time evolution of a distribution of stars (white dots) under the influence of an oscillating filament (represented as the red density profile) from Boekholt et al. (2017). The simulations have a fixed oscillation period of $P = 2\,\mathrm{Myr}$ but varying amplitude: $A = 0.5\,\mathrm{pc}$ (top row), $A = 1.25\,\mathrm{pc}$ (middle row) and $A = 2.5\,\mathrm{pc}$ (bottom row). The simulations show that an amplitude of $A = 1.25\,\mathrm{pc}$ results in a symmetric distribution of ejected stars.

succesfully reproduce the symmetric distribution of stars around the filament, but assume a simple motion of the filament. To get a more robust result, one would have to consider the gravitational interactions of the stars in the cluster (see Matus-Carrillo et al. in prep.) and more complex filament motions (e.g., rotation, magnetic tension and instabilities).

MHD instabilities in the gas are expected to arise from a helical field morphology. Schleicher and Stutz (2018) show that the magnetic tension can give rise to a filament oscillation in the ISF, consistent with the observed kinematic timescales ($\sim 1.45\,\mathrm{Myr}$). This is possible considering that the magnetic and rotational energy may be comparable to the gravitational potential energy.

Near the center of the ONC lies a massive dense core called OMC1. This core hosts a powerful outflow with mass around $\sim 10\,\mathrm{M}_\odot$ and velocities of $v \sim 30 - 10\,\mathrm{km\,s^{-1}}$ (Zinnecker and Yorke, 2007). The outflow originates near the center of the cluster in the BN/KL region (Becklin and Neugebauer, 1967; Kleinmann and Low, 1967), caused by a powerful explosion after close interaction between two or more protostars about $\sim 500\,\mathrm{yr}$ ago (Zapata et al., 2009; Bally et al., 2017). Figure 2.12 shows the BN/KL outflow morphology traced by the high velocity ^{12}CO $(2-1)$ emission and the shock-excited H_2 and [Fe II] emission from Bally et al. (2017).

Position velocity (PV) diagrams derived from observations of ^{12}CO $(1-0)$ and ^{13}CO $(1-0)$ of the ISF from Kong et al. (2018) show a wave-like morphology along the filament. Figure 2.13 shows the PV diagram of the ^{13}CO emission along the ISF from Kong et al. (2018). The wave-like morphology is seen from the change in velocity along the filament, specifically the northern region of the ISF (offset 42 to 0 in Figure 2.13) where the observed velocity rises from $v \sim 8\,\mathrm{km\,s^{-1}}$ (at offset 42) to $v \sim 12\,\mathrm{km\,s^{-1}}$ (at offset ~ 21), then goes down again to $v \sim 8\,\mathrm{km\,s^{-1}}$ at offset ~ 3 producing an arch pattern of velocity reminiscent of an oscillation or wave. In the southern region of the filament (offset 0 to 42 in Figure 2.13) the velocities are also reminiscent of a wave, presenting changes in the direction of the velocity gradient and arched patterns that fluctuate between $v \sim 7 - 11\,\mathrm{km\,s^{-1}}$. The observed morphology is not consistent with a propagating wave because the position maximum displacement coincides with the position of maximum velocity (Kong et al., 2018). The global velocity structure seen in these diagrams is represented by a blueshifted velocity gradient towards the OMC1 region, this feature is also seen in the high density gas of the filament (see Friesen et al. 2017; Hacar et al. 2017). The figure also shows that the broad velocity spread at the reference position reflects the explosive outflow in the Orion BN/KL region (Kong et al., 2018).

Observations carried out with IRAM 30 m of N_2H^+ $(1-0)$ of the ISF display a similar velocity gradient, the observations suggest that there is an accelerated inflow of material towards the ONC (Hacar et al., 2017). A higher resolution study with ALMA observations of the same molecular transition revealed the presence of velocity coherent fibers that trace the distribution of cores and protostars (Hacar et al., 2018). The fibers are organized in a hub-like association and their orientation follows the local gravitational potential (Hacar et al., 2018). The inflow of

material towards the ONC reflects the global collapse of the OMC1 region (Hacar et al., 2017).

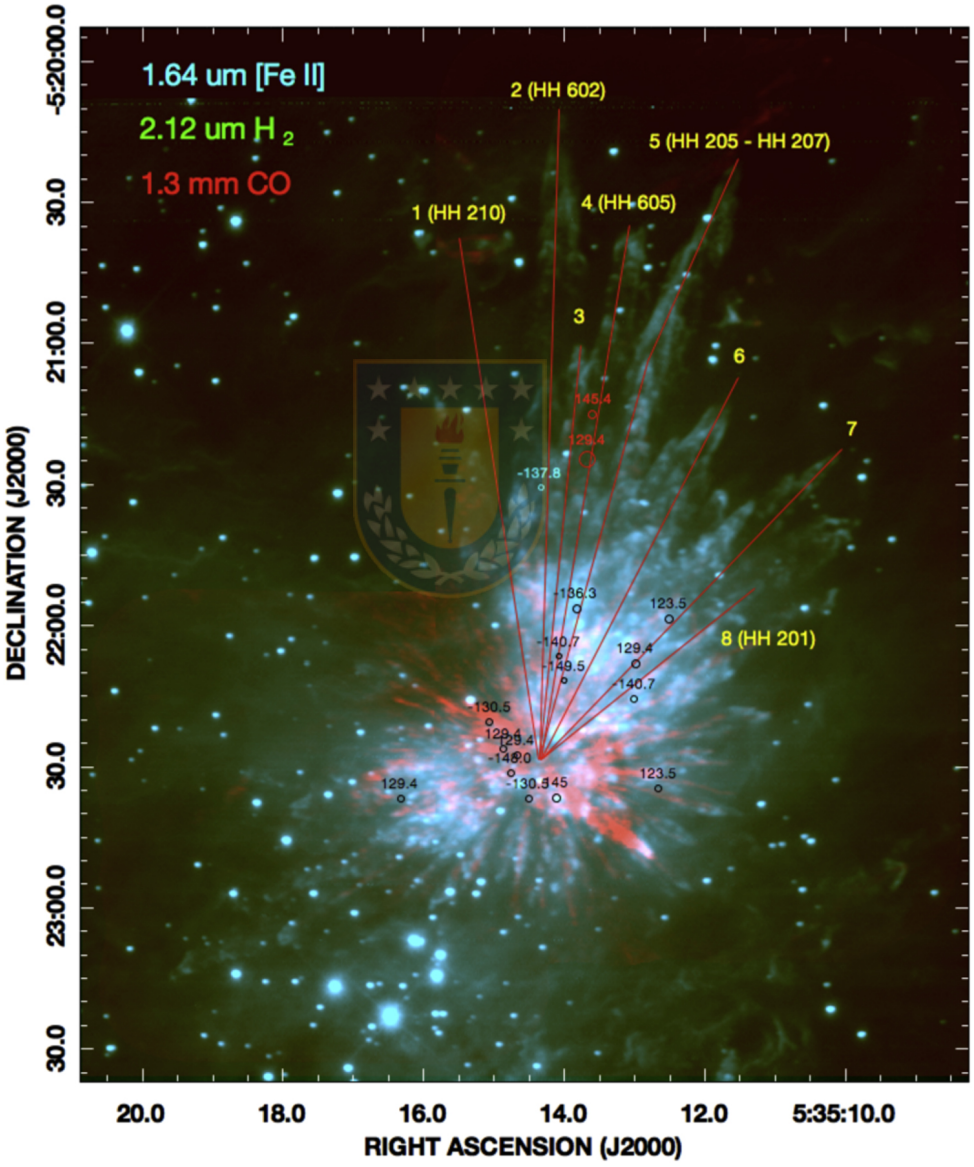

Figure 2.12: ^{12}CO $(2-1)$ ALMA maps in the redshifted and blueshifted radial velocity ranges that cover the high velocity emission from -100 to $+120\,\mathrm{km\,s^{-1}}$ (red), superimposed on the $2.12\,\mu$m shock-excited H_2 (green) and [Fe II] emission (blue) from the OMC1 outflow (Bally et al., 2017). The red lines indicate the prominent H_2 and [Fe II] 'fingers'.

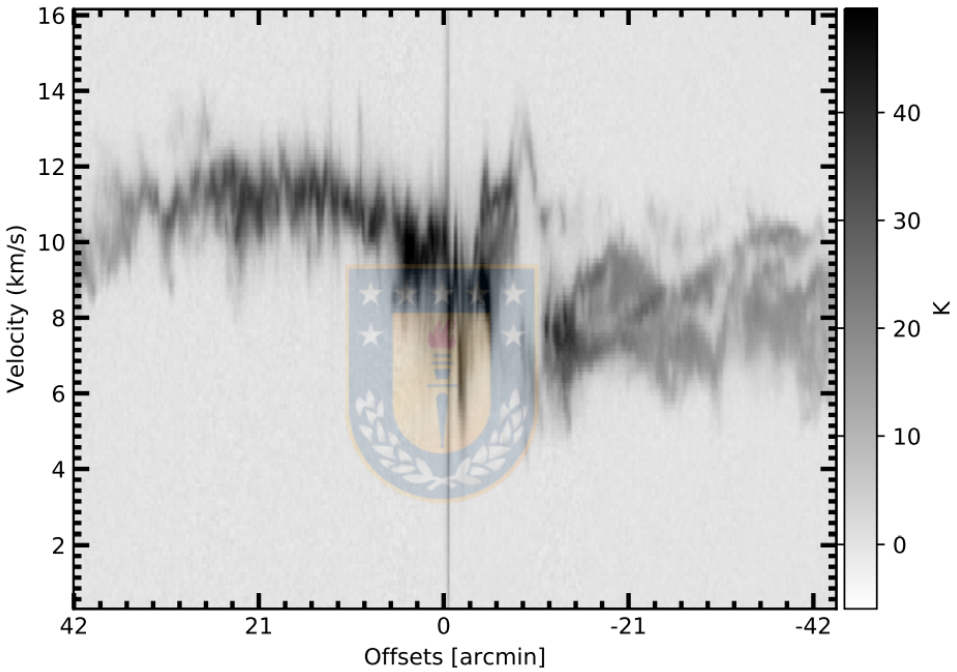

Figure 2.13: PV diagram of the ^{13}CO emission along the ISF from Kong et al. (2018). The offset reference coincides with the position of the Orion BN/KL region.

Chapter 3

Data

A description of the visualization methods and the datasets used in this work is given below. All data is publicly available and focuses on the ISF (Bally et al., 1987; Stutz and Gould, 2016) region of the Orion A molecular cloud, where the ONC (M42) is forming.

3.1 Spectral line data cubes

Spectral data cubes represent the data type obtained from observations carried out using integrated field spectroscopy, which produces a spectrum for each point in space (limited by spatial resolution) observed. This work focuses on molecular line observations obtained with radiotelescopes equiped with integral field units.

Data cubes contain celestial and spectral coordinates, the spectral axis is represented in terms of the radial velocity at the local standard rest (which considers the motion of the Sun) corresponding to the Doppler shift of the line. The spectral axis is divided by a given number of velocity channels, which determine the spectral resolution of the observation.

To visualize the information contained in spectral data cubes we usually make projections or extract slices from the cube such as, obtaining a spectrum at a given location, extracting a slice along a spatial or spectral axis or generating moment maps of different orders (operation that involves integrating the cube over an axis).

Moment maps are obtained by collapsing the data cube over an axis, usually chosen to be the spectral axis. The moment maps used in this work are described in the CASA[1] and SpectralCube[2] documentation:

[1] `https://casa.nrao.edu/docs/casaref/image.moments.html`

[2] `https://spectral-cube.readthedocs.io/en/latest/moments.html`

- Moment 0: Corresponds to the integrated value of the chosen axis. Integrating over the spectral axis results in the velocity integrated emission map. Integrating over a spatial axis results in an integrated 2D projection of the other two coordinates (position and velocity). The moment 0 is given by

$$M_0 = \Delta v \sum_i^n I_i, \tag{3.1}$$

  where Δv is the size of the channel or pixel, I_i is the value of the ith pixel and n is the total number of pixels in the given axis.

- Moment 1: Corresponds to the intensity weighted mean coordinate. It is tipically used to obtain centroid velocity maps. The moment 1 is given by

$$M_1 = \frac{\sum_i^n I_i v_i}{M_0}, \tag{3.2}$$

  where v_i is the coordinate of the ith pixel (usually the velocity).

- Moment 2: Corresponds to the intensity weighted dispersion and is typically used to obtain velocity dispersion and linewidths. The moment 2 is given by

$$M_2 = \sqrt{\frac{\sum_i^n I_i (v_i - M_1)}{M_0}}. \tag{3.3}$$

Higher order moments are used to extract other different statistical parameters not relevant to this work, they are computed as described in the SpectralCube documentation:

$$M_N = \frac{\sum_i^n I_i (v_i - M_1)^N}{M_0}, \tag{3.4}$$

where N is the order.

In this work, moment maps are computed using the Python module `SpectralCube`, in which routines to compute moment maps by specifying the data cube, the moment order and the axis of integration are implemented, among other routines useful for data cube handling and visualization. More details on the module are described in the documentation website (see also Ginsburg et al. 2015).

3.2 Gas and stellar mass maps

To quantify the gas mass distribution, we use the column density N(H) map from Stutz (2018). This map was derived from the *Herschel* dust emission at 160 μm, 250 μm, 350 μm, and 500 μm (Stutz and Kainulainen, 2015) with a resolution of $\sim 20''$, corrected in the center of the ONC

using APEX 870 μm data due to saturation in Stutz (2018). The N(H) data corresponds to the total hydrogen column density, where N(H) = 2 × N(H_2) (see Stutz and Kainulainen 2015 for more details).

The stellar mass distribution corresponds to the Stutz (2018) stellar mass map. This map was constructued by counting young stellar objects (YSOs) identified with *Spitzer* from Megeath et al. (2016). To compute the stellar mass, Stutz (2018) assumed a disk fraction of 0.75 (Megeath et al., 2016) and a stellar mass of 0.5 $M_\odot$ (Kroupa, 2001).

3.3 ^{12}CO $(1-0)$ and ^{13}CO $(1-0)$ data

We use the ^{12}CO (1−0) and ^{13}CO (1−0) observations from Ripple et al. (2013). The observations were carried out with the Five College Radio Astronomy Observatory 14 meter telescope during 2005 and 2006. The Full Width Half Maximum (FWHM) of the beam is 45" for ^{12}CO and 47" for ^{13}CO. The spectral resolution of each data cube is 0.077 km s^{-1} for ^{12}CO and 0.08 km s^{-1} for ^{13}CO. The 1σ errors due to thermal noise within 0.2 km s^{-1} wide channels are 2.0 K for ^{12}CO and 0.77 K for ^{13}CO, as reported in Ripple et al. (2013). We refer the reader to Ripple et al. (2013) for further details of this dataset. The critical density of the ^{12}CO $(1-0)$ transition is about 740 cm^{-3} and 1.9×10^3 cm^{-3} for ^{13}CO $(1-0)$ (Wilson et al., 2009; Hernandez and Tan, 2011).

Figure 3.1 shows the velocity integrated intensity maps of ^{12}CO and ^{13}CO respectively. The maps were integrated over a velocity range between $v_{\rm LSR} = 0$ km s^{-1} to $v_{\rm LSR} = 16$ km s^{-1}. The blue box indicates the region that the N_2H^+ observation covers and the blue curve represents the dust ridgeline from Stutz (2018). We observe from these figures high emission from the filamentary regions that are the typical sites of recent star formation, with kinetic temperatures of $T_k \sim 25$ K (Ripple et al., 2013). Also, there is extended faint emission that surrounds the main ridge of the filament in both tracers.

3.4 N_2H^+ $(1-0)$ data

We use observations of N_2H^+ (1−0) from Tatematsu et al. (2008) carried out with the Nobeyama Radio Observatory 45 m telescope between 2005 and 2007. The FWHM is ∼ 17" at 93GHz. The spectral resolution of this data cube is 0.12 km s^{-1}. The N_2H^+ $(1-0)$ transition has a critical density of 6.1×10^4 cm^{-3} assuming a kinetic temperature of 10 K (Shirley, 2015). We refer the reader to Tatematsu et al. (2008) for further details of this dataset.

The left pannel of Figure 3.2 shows the complete velocity integrated emission of N_2H^+, which covers the ISF region (northern portion of the Orion A cloud). This figure represents the dense and clumpy structure of the filament gas that is less affected by star formation activity, such as outflows (Tatematsu et al., 2008). This gas is colder than both CO isotopologues with

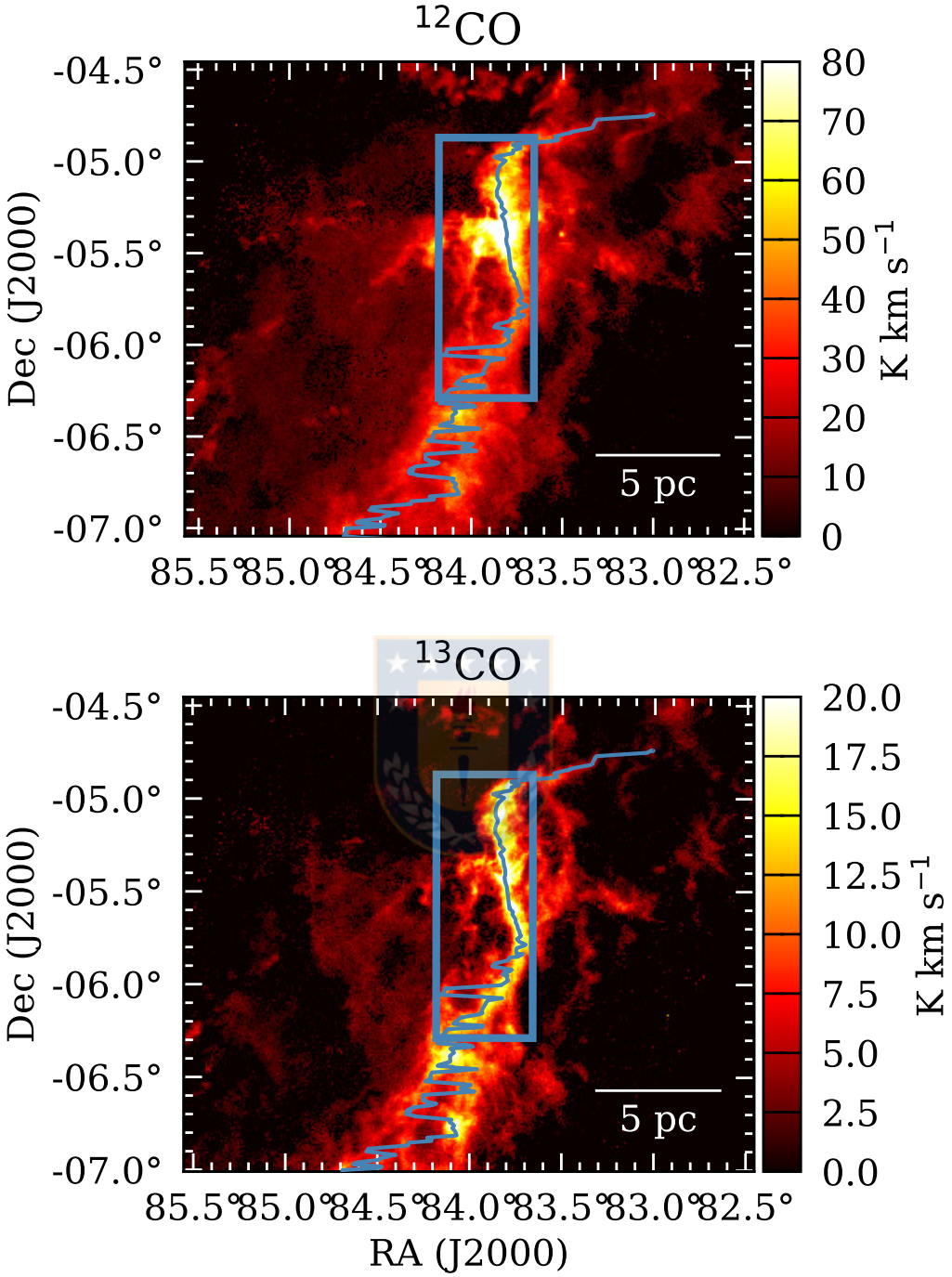

Figure 3.1: ^{12}CO $(1-0)$ (top) and ^{13}CO $(1-0)$ (bottom) integrated intensity maps of the Orion A region, from Ripple et al. (2013). The maps were integrated over a velocity range from $v_{\rm LSR} = 0\,{\rm km\,s^{-1}}$ to $v_{\rm LSR} = 16\,{\rm km\,s^{-1}}$. In both panels the blue curve is the column density ridgeline (Stutz, 2018) and the blue box indicates the region that the N_2H^+ observation field covers, that is, the ISF. A 5 pc scale-bar is shown at the bottom of each panel.

typical kinetic temperatures of the cores of around $T \sim 20\,\mathrm{K}$ (Tatematsu et al., 2008). This dense structure is embedded in the less dense gas traced by CO and represents the well of the gravitational potential in this work, because of its very good agreement with the column density inferred from the dust emission (not shown here) and the derived dust ridgeline from Stutz (2018).

3.5 NH_3 data

We use the first public release of the Green Bank Ammonia Survey (GAS) observations from Friesen et al. (2017) of the Orion A North region. These correspond to the NH_3 $(1,1)$, $(2,2)$ and

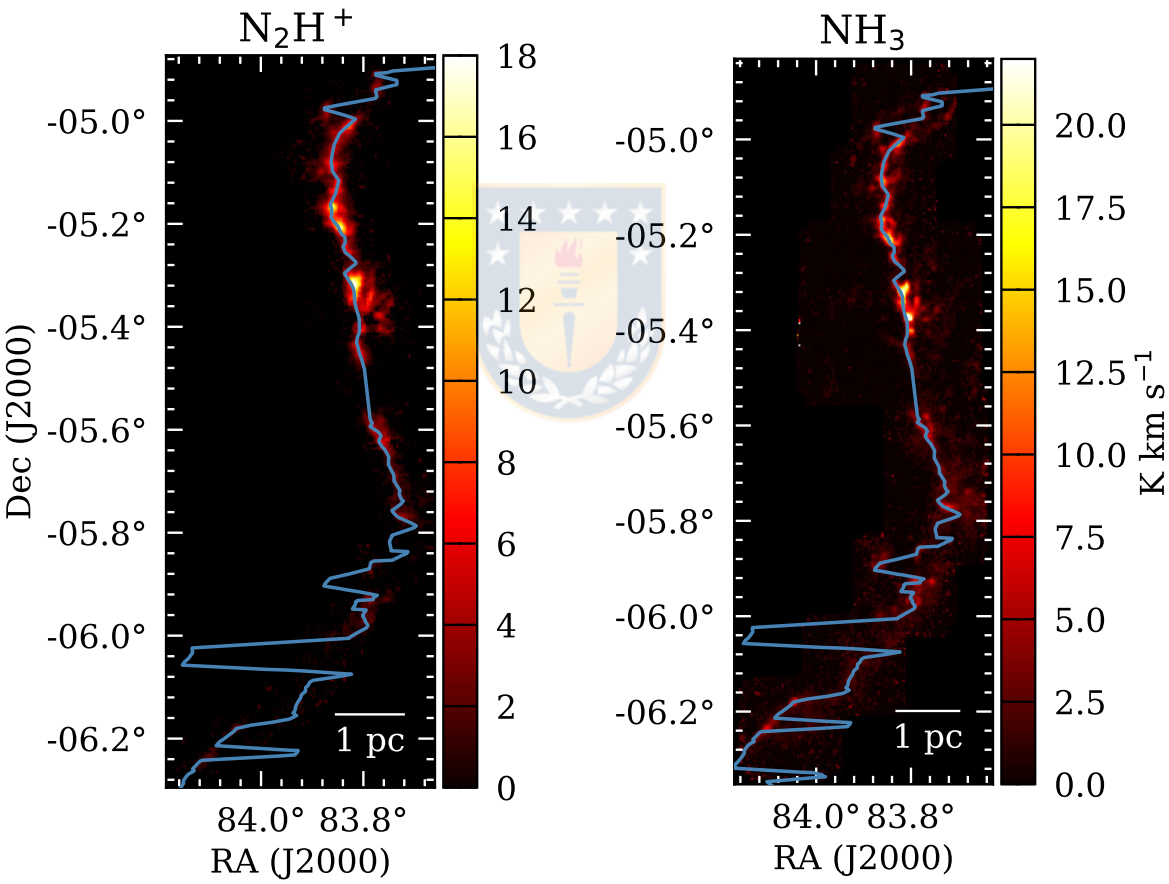

Figure 3.2: *Left*: N_2H^+ $(1-0)$ integrated intensity map of the ISF region from Tatematsu et al. (2008). *Right*: NH_3 $(1,1)$ velocity integrated emission map of the ISF region from Friesen et al. (2017). A 1 pc scalebar is shown at the bottom of each panel. The blue curve is the column density ridgeline (Stutz, 2018). The area covered by the N_2H^+ map corresponds to the blue box in Figure 3.1.

$(3,3)$ transitions with a spectral resolution of $\sim 0.07\,\mathrm{km\,s^{-1}}$ and beamsize of $\sim 32''$ at 23.7 GHz, corresponding to the NH_3 $(2,2)$ rest frequency. For more details of the datasets and analysis see Friesen et al. (2017). NH_3 has a critical density of $\sim 2 \times 10^3\,\mathrm{cm^{-3}}$ assuming a kinetic temperature of 10 K (Shirley, 2015). The resulting maps of interest here are the integrated intensity and centroid velocity. These maps are obtained from NH_3 line fitting analysis using the Python package PySpecKit (Ginsburg and Mirocha, 2011). We refer the reader to Section 3 of Friesen et al. (2017) for further details in the NH_3 line fitting.

The right pannel of Figure 3.2 shows the velocity integrated emission of the NH_3 $(1,1)$ transition from Friesen et al. (2017) of the ISF. The figure highlights the close resemblance with the N_2H^+ clumpy emission but with more faint extended emission than N_2H^+. We see that all tracers shown above follow closely the dust ridgeline from Stutz (2018), therefore we use it to trace the center of the filament throughout this work.

3.6 Point sources

We use several protostar and point source catalogs to compare their positions to the radial velocity structure of the ISF (see Section 5.5). The protostar selection is limited to the ISF region: the *Herschel* Orion Protostar Survey (HOPS, Stutz et al. 2013; Furlan et al. 2016), protostellar cores observed with ALMA at 3 mm continuum of the northern part of the ISF from Kainulainen et al. (2017), protostellar cores identified in the OMC1 North region observed with the Submillimeter Array (SMA) at 1.3 mm from Teixeira et al. (2016), and the outflow source in the Orion KL region from Zapata et al. (2009) observed with the SMA.

Chapter 4

Analysis

We aim to study the kinematics of the ISF at different gas densities. In order to do this, we extract the 3 principal parameters from each spectrum: integrated intensity, velocity centroid and linewidth.

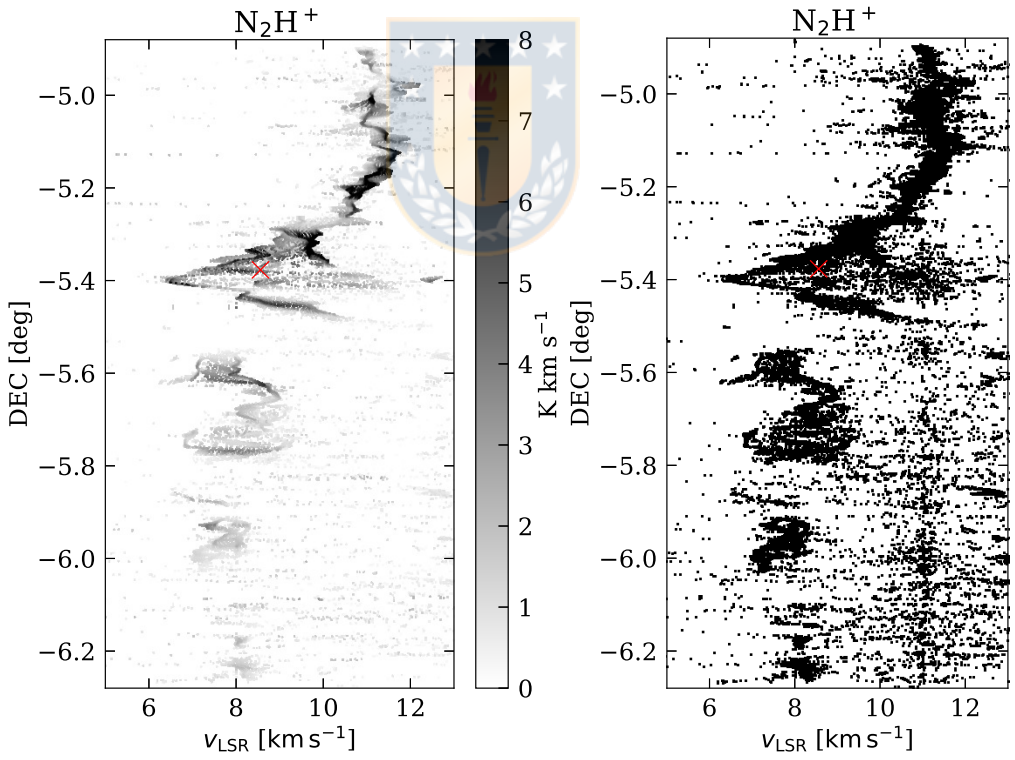

Figure 4.1: *Left*: N_2H^+ intensity-weighted velocity centroid as a function of δ. *Right*: N_2H^+ position-velocity diagram of the velocity centroid as a function of δ, without intensity weighting. The red ×-symbol denotes the center of mass coordinate of the ONC stars and the mean velocity of the cluster stars Stutz (2018). The intensity-weighted diagram (left) enables us to identify structures that are either muddled or invisible in the right panel.

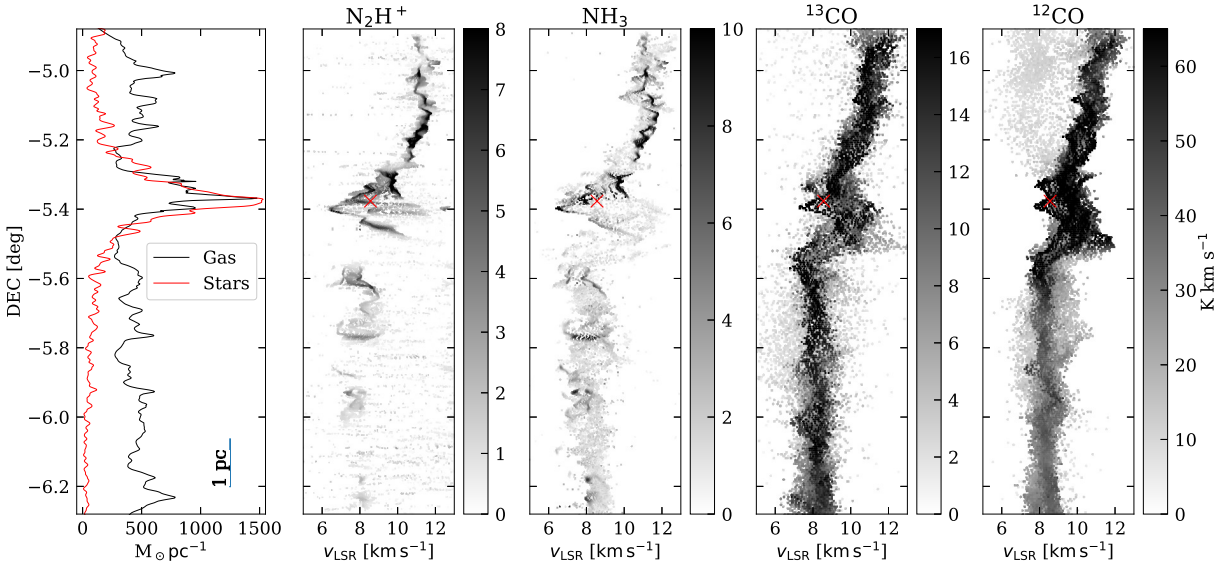

Figure 4.2: From left to right: Mass per unit length as a function of δ of the gas (black curve) from Stutz (2018) and young stars (red curve) from Megeath et al. (2016) in the ISF; intensity-weighted velocity centroid as a function of Declination for N_2H^+, NH_3, ^{12}CO and ^{13}CO, respectively. The position-velocity centroid (PV) diagrams are obtained from the integrated emission and velocity centroid maps for all tracers (see text). All diagrams are extracted within the N_2H^+ observation area (see Figure 3.2), with an R.A. range of $83.66° < \alpha < 84.18°$ (the region indicated as the blue box in Figure 3.1). The red $\times$-symbol denotes the center of mass coordinate of the ONC stars and the mean velocity of the cluster stars Stutz (2018). The N_2H^+ and NH_3 PV structures are remarkably similar, and clearly illustrate the small-scale velocity structure in the ISF (see text). A blue-shifted velocity peak near the cluster position is seen in all tracers at Decl. $\sim -5.4°$. A hint of a double velocity component is already visible in the ^{12}CO PV diagram (see Section 5.4).

With the first two parameters, we study the velocity structure along the filament by constructing intensity-weighted position-velocity diagrams. These diagrams are shown in Figure 4.1 and the second to fifth panel of Figure 4.2 for N_2H^+, NH_3, ^{13}CO and ^{12}CO respectively. The PV diagrams are shown alongside the mass per unit legth distribution of the stars and gas along the filament, shown in the first panel of the same figure. All PV diagrams are extracted from the same area with N_2H^+ coverage (the blue box shown in Figure 3.1), all emission outside this region is excluded.

Our method uses the velocity integrated emission and the line velocity centroid in order to reduce noise and highlight the salient velocity structure in the plane of the sky. A comparison of our intensity-weighted mehod and the PV diagram with no weighting is shown in Figure 4.1, our method highlights large and small scale velocity structure of the ISF. We see from Figure 4.2 that in all tracers, the velocities follow a North to South gradient that grows towards lower velocities

and terminates with a blue-shifted velocity peak near the center of the cluster. This peak is located close to the peak of the mass distribution of gas and stars, which seem concentrated around the cluster region. We also observe from Figure 4.2 that all tracers have similar global kinematics but present unique small scale structures, such as peaks and waves, highlighting analogy between dense tracers (N_2H^+ and NH_3) and lower density tracers (^{13}CO and ^{12}CO). We also plot the position of the center of mass and mean velocity of the ONC (Stutz, 2018) with a $\times$-symbol and see that the blue shifted velocity peak seen in all tracers contains the position of the cluster.

A more detailed analysis of the results and interpretations from Figure 4.2 is presented in Section 5.1.

We also present analysis and results of the linewidths, global velocities and protostellar feedback in Chapter 5.

Below we describe how we obtain the kinematic parameters and construct the PV diagrams from Figure 4.2 for each tracer.

4.1 N_2H^+

In order to obtain the kinematic parameters of the N_2H^+ $(1-0)$ hyperfine line structure, we performed a fit of the N_2H^+ spectra with the Python module PySpecKit (Ginsburg and Mirocha, 2011). The module includes a built-in N_2H^+ fitter. The fitter produces a model hyperfine spectrum that consists of multiple Gaussian components and fits all hyperfine components simultaneously. The fitter uses the de-excitation rate coefficients from Daniel et al. (2005) to determine the model spectrum considering fits of both the de-excitation rotational parameters and average opacity. Figure 4.3 shows an example of the fitting results of one sprectum in our data.

The fitter requires an errormap, a list or cube of starting values for the parameters, and a signal to noise threshold. We determine the errormap from emission-free channels between $v_{LSR} = [-3.65\,\mathrm{km\,s^{-1}}, -0.35\,\mathrm{km\,s^{-1}}]$.

We tested the fitter response to different noise levels in order to choose a global signal to noise threshold. For this we performed a Monte Carlo analysis of the fitted linewidth, by picking a spectrum with a high signal to noise ratio ($S/N = 11$) and adding random gaussian noise. The dispersion of the added noise distribution is given by $\sigma = i\sigma_0$, where $\sigma_0 = 0.0648\,\mathrm{km\,s^{-1}}$ is the noise (rms value) of the chosen spectrum and i is a number ranging from 1 to 4 in intervals of 0.05 (representing different noise levels). We then transformed the total sigma values ($\sigma^2_{TOT} = \sigma^2_0 + \sigma^2$) into signal to noise ratio values. The process is repeated $N = 1000$ times for each noise level. We found that a value of $S/N = 4$ produced consistent fitted linewidth values. Higher values of the S/N produced no change in the fitted value and its associated error. We therefore adopt the $S/N = 4$ threshold throughout our N_2H^+ hyperfine fitting procedure.

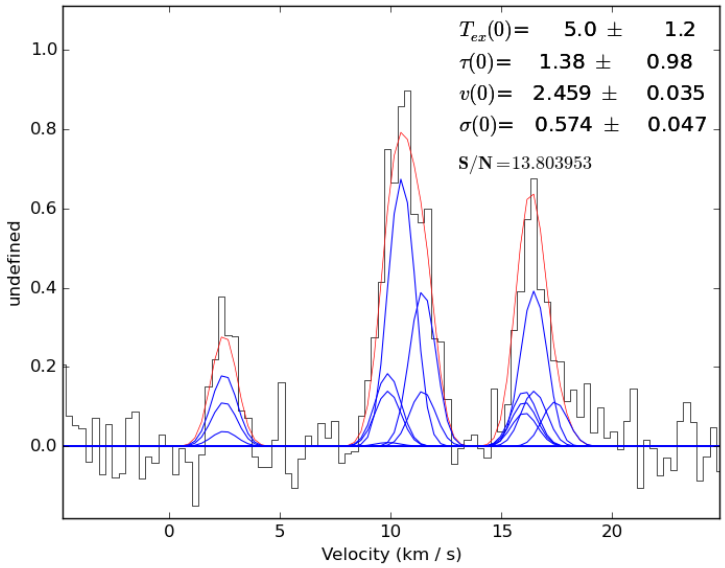

Figure 4.3: Example of a fitted spectrum in our data. The black curve is the real data, rhe red curve represents the resulting fit and the blue curves represent the different gaussian components used to obtain the fit. In the top right corner the different fitted parameters are shown: excitation temperature (T_{ex}) in K, opacity (τ), central velocity (v) in km s^{-1} and linewidth (σ) in km s^{-1}. The signal to noise ratio of the specturm is also shown with the parameters.

Figure 4.4 shows the mean fitted linewidth and its corresponding errorbar for each noise level as a function of the signal to noise ratio resulting from the Monte Carlo analysis. We find that the model spectra residuals are consistent with observational noise and conclude that the fitting procedure reproduces the observed spectra well.

We follow this fitting procedure to retrieve the principal kinematic parameters that we are interested in: central line velocity, linewidth and integrated intensity, and their respective errors. We also generate excitation temperature and optical depth values, but defer analysis of these later parameters to a future investigation.

We used the fitted central velocity map and integrated intensity map to generate an intensity weighted PV diagram, see the second panel of Figure 4.2. For this we extract the integrated intensity and central line velocity as a function of Declination, weighted by the integrated intensity.

4.2 NH_3

We use the NH_3 $(1,1)$ integrated intensity map and the velocity $v_{\rm LSR}$ map of the ISF from Friesen et al. (2017). Panel 3 of Figure 4.2 shows the intensity-weighted PV diagram for NH_3.

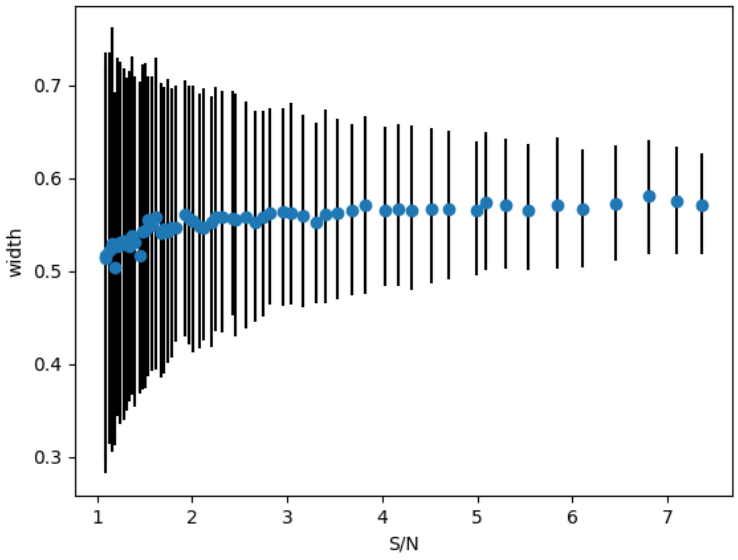

Figure 4.4: Plot of the mean fitted width parameter (in $\mathrm{km\,s^{-1}}$) with its corresponding errorbar resulting from the montecarlo analysis versus the signal to noise ratio of the spectrum. The plot shows that the errorbars remain consistent when the signal to noise ratio is above 4.

We highlight the similarity between the small-scale structures in both NH_3 and N_2H^+; the fact that these two datasets were acquired, analyzed, and tabulated completely independently indicates that the small-scale structures present in both are robust (see discussion below).

4.3 ^{12}CO and ^{13}CO

We begin by setting a 4σ minimum signal threshold for each spectrum. In order to do this we generate a noise map by computing the standard deviation of line-free velocity channels between $v_{LSR} = [-10\,\mathrm{km\,s^{-1}}, -2\,\mathrm{km\,s^{-1}}]$ for each spectrum. We then consider only spectra with a maximum value $\geq 4\sigma$. We then derive the respective velocity integrated intensity maps, radial velocity centroid maps and velocity dispersion maps using the Python module `SpectralCube`[1]. The integrated intensity maps for ^{12}CO and ^{13}CO are integrated over $v_{LSR} = [0\,\mathrm{km\,s^{-1}}, 16\,\mathrm{km\,s^{-1}}]$ and shown in Figure 3.1.

We used the velocity maps and intensity maps to generate intensity weighted PV diagrams for ^{12}CO and ^{13}CO, shown in the fourth and fifth panel of Figure 4.2. For this we extract the velocity integrated emission and line velocity centroid values at each position, and then plot the velocity centroids as a function of Declination weighted by the integrated intensity, as described for the other tracers.

[1] `https://github.com/radio-astro-tools/spectral-cube`

Chapter 5

Results: Velocity structure of the ISF

In this chapter we will discuss the main features apparent in the gas velocity data, starting with the global appearance of Figure 4.2. We use the kinematic parameters, the line centroid velocities and linewidths, extracted as described in Chapter 4.

5.1 Position-velocity structure as a function of density

Here we focus on Figure 4.2. All plots shown in this diagram were extracted within $83.66° < \alpha < 84.18°$, the region indicated as the blue box in Figure 3.1. The first panel of Figure 4.2 shows the mass per unit length (M/L) distribution of the gas (black curve) and young stars (red curve) along the ISF as a function of δ. The mass distribution of stars and gas (see 3) in this diagram is concentrated near the ONC region (Stutz and Gould, 2016; Stutz, 2018). Due to the restricted range over which we extract the M/L profiles, the gas peak near the center of the ONC is prominent (see 5.2 for a comparison between the gas potential and gas velocities). The mass of the gas dominates over the rest of the filament. Panels 2 to 5 of Figure 4.2 show the radial velocity centroid of the lines as a function of Declination for each tracer, sorted in order of descending critical density value (see Chapter 3). The figures represent the distribution of mean line velocities along the filament, ignoring line of sight features (such as multiple line components). Therefore these give us information of the plane of the sky mean velocity distribution. Figure 4.2 shows with a red $\times$-symbol the position of the center of mass and mean velocity of the ONC (Stutz, 2018).

The second panel of Figure 4.2 shows the N_2H^+ PV diagram of the ISF. The global structure of the dense filament seems to be concentrated along the filament axis with little spread in velocities at each δ. The velocity structure of N_2H^+ is characterized by a curving velocity gradient going from $v_{\rm LSR} \sim 11\,{\rm km\,s^{-1}}$ in the north region to $v_{\rm LSR} \sim 7\,{\rm km\,s^{-1}}$ in the ONC. South

of the ONC, the velocity of N_2H^+ is approximately constant at $v_{\rm LSR} \sim 8\,{\rm km\,s^{-1}}$. Just south of the ONC, at $\delta \sim -5.5°$ the dense filament is broken, developing a region without significant N_2H^+ emission. This region presents a jump in velocity between both ends of the filament of about $\Delta v_{\rm LSR} \sim 2\,{\rm km\,s^{-1}}$. This break just below the ONC was highlighted by Stutz (2018) and interpreted as an indication that the instabilities that are giving rise to the general velocity structure in the ISF are propagating from North to South through the filament (Stutz et al., 2018b). Hacar et al. (2017) show a similar analysis of the N_2H^+ velocity structure in the ISF. They found a velocity gradient in the proximity of the ONC with values up to $5-7\,{\rm km\,s^{-1}\,pc^{-1}}$, and suggest that the gas is gravitationally accelerated towards the center of the forming cluster. The velocities of N_2H^+ near the center of the OMC1 region ($\delta \sim -5.4°$) appear with a broad dispersion of around $v_{\rm LSR} \sim 3\,{\rm km\,s^{-1}}$. We observe small scale velocity fluctuations along the filament. Most of the emission appears confined to the blue-shifted main peak structure with a narrow range in velocities. As shown by the PV point for the ONC (red $\times$-symbol), the ONC star cluster has a mean velocity and postion that is offset from the dense filament gas as traced by N_2H^+. The small-scale velocity fluctuations along the filament have a morphology analogous to wrapping or rotating structures, and persist most obviously along the entire Northern portion of the ISF.

The third panel of Figure 4.2 shows the NH_3 PV diagram of the ISF. We observe the same North to South velocity gradient seen in N_2H^+ from $v_{\rm LSR} \sim 11\,{\rm km\,s^{-1}}$ and terminating in the ONC region with $v_{\rm LSR} \sim 7\,{\rm km\,s^{-1}}$. The similarities between the velocity structures, at small and large scale, of NH_3 and N_2H^+ are stricking considering their different critical densities (see Chapter 3). For NH_3 it is also possible to observe that the filament is interrupted around $\delta \sim -5.5°$, but the N_2H^+ break region contains some faint NH_3 emission, consistent with the presence of lower density gas in the region where the dense gas filament is broken.

The fourth panel of Figure 4.2 shows the ^{13}CO PV diagram of the ISF. The distribution of velocities at each δ appear much broader than in N_2H^+ and NH_3, with a spread of $v_{\rm LSR} \sim 1-2\,{\rm km\,s^{-1}}$ across the filament. We observe a similar North to South velocity gradient as in N_2H^+ and NH_3 (see also Kong et al., 2018, and Kong et al. (in prep)) with the most blue-shifted velocity component of about $v_{\rm LSR} \sim 8\,{\rm km\,s^{-1}}$ around the ONC region. Around the ONC region we observe two blue-shifted velocity peaks at $v_{\rm LSR} \sim 8\,{\rm km\,s^{-1}}$ and a faint red-shifted velocity component at $\delta \sim -5.5°$. The filament appears as one coherent structure with no signs of fragmentation. The ^{13}CO emission bridges the gap seen at higher densities and there is a red-shifted velocity component with a peak morphology near $\delta \sim -5.5°$.

The fifth panel of Figure 4.2 shows the ^{12}CO PV diagram of the ISF. We observe a north to south velocity gradient from $v_{\rm LSR} \sim 12\,{\rm km\,s^{-1}}$ in the north region to $v_{\rm LSR} \sim 8\,{\rm km\,s^{-1}}$ in the ONC region. Around the ONC region we see two blue-shifted velocity peaks, similar to ^{13}CO, with velocities $v_{\rm LSR} \sim 8\,{\rm km\,s^{-1}}$. The red-shifted velocity component seen in ^{13}CO at $\delta \sim -5.5°$

is now a clear structure with a red-shifted velocity peak of $v_{\rm LSR} \sim 12\,{\rm km\,s^{-1}}$. The filament as traced by ^{12}CO does not show any signs of the N_2H^+ break, similar to ^{13}CO. The velocity structure of ^{12}CO presents small scale velocity fluctuations along the filament. We observe a faint but coherent and extended blue-shifted velocity component in the northern region of the ISF at a velocity of about $v_{\rm LSR} \sim 8\,{\rm km\,s^{-1}}$. This feature is only present in the ^{12}CO PV diagram, we carry out further analysis of it in Section 5.4.

We observe that all tracers show a North to South velocity gradient starting from Declination $\sim -5.0°$ with velocity $v_{\rm LSR} \sim 11\,{\rm km\,s^{-1}}$, terminating with a blue-shifted velocity peak of $v_{\rm LSR} \sim 7-8\,{\rm km\,s^{-1}}$ at Declination $\sim -5.4°$. The peak of the stellar and total gas-mass profiles, as well as the center of mass of the ONC, are located $\sim$ 0.2 pc to north of the blue-shifted velocity peaks seen in the PV diagrams (see also Stutz, 2018). The velocity gradient in the proximity of the ONC is found to be about $5-7\,{\rm km\,s^{-1}\,pc^{-1}}$ from N_2H^+ observations and suggests that the dense gas is accelerated towards the center of the OMC1 region (Hacar et al., 2017). We see that south of the OMC1 region the velocity of the filament remains constant with $v_{\rm LSR} \sim 8\,{\rm km\,s^{-1}}$ for all tracers. The appearance of out PV diagrams is consistent with the Kong et al. (2018) PV diagrams extracted from higher resolution ^{13}CO data (see Figure 2.13). Moreover, the N_2H^+ and NH_3 data present small-scale structures similar in both tracers. These structures are also present in the Kong et al. (2018) diagrams and have been previously interpreted as rotational features or possible wave signatures on small scales (Stutz et al., 2018a).

5.2 Velocity dispersion radial profiles

Figure 5.1 shows the average non-thermal velocity dispersion and Mach number radial profiles of the four tracers considered for two regions in the ISF. The two regions were identified from the ^{12}CO PV diagram from Figure 4.2, and correspond to the northern ISF region, from $\delta = -4.9° \rightarrow \delta = -5.25°$, and the ONC region from $\delta = -5.25° \rightarrow \delta = -5.48°$. The ONC region is chosen to enclose the blue-shifted velocity peak seen in the four tracers (see Section 5.1). The two regions are represented with different colors in Figure 5.1, the northern region is indicated with red curves and the cluster region is represented with gray curves.

The velocity dispersion profiles are computed using the second moment from both CO isotopologues and the fitted linewidth from NH_3 and N_2H^+. The profiles are extracted relative to the central axis of the filament as represented by the dust ridgeline from Stutz and Gould (2016). This ridgeline shows excellent correspondence to ^{13}CO, NH_3 and in particular with the N_2H^+ emission (see Figures 3.1 & 3.2); therefore we adopt the Stutz (2018) ridgeline as a robust tracer of the bottom of the gravitational potential well of the ISF.

To investigate the non-thermal linewidth profiles, we must subtract the thermal contribution. We compute the non-thermal velocity dispersion component as $\sigma_{\rm NT} = \sqrt{\sigma^2_{obs} - \frac{kT_{\rm k}}{m}}$ (Liu et al., 2019), where $T_{\rm k}$ is the kinetic temperature and m is the mass of the species. Here we assume the

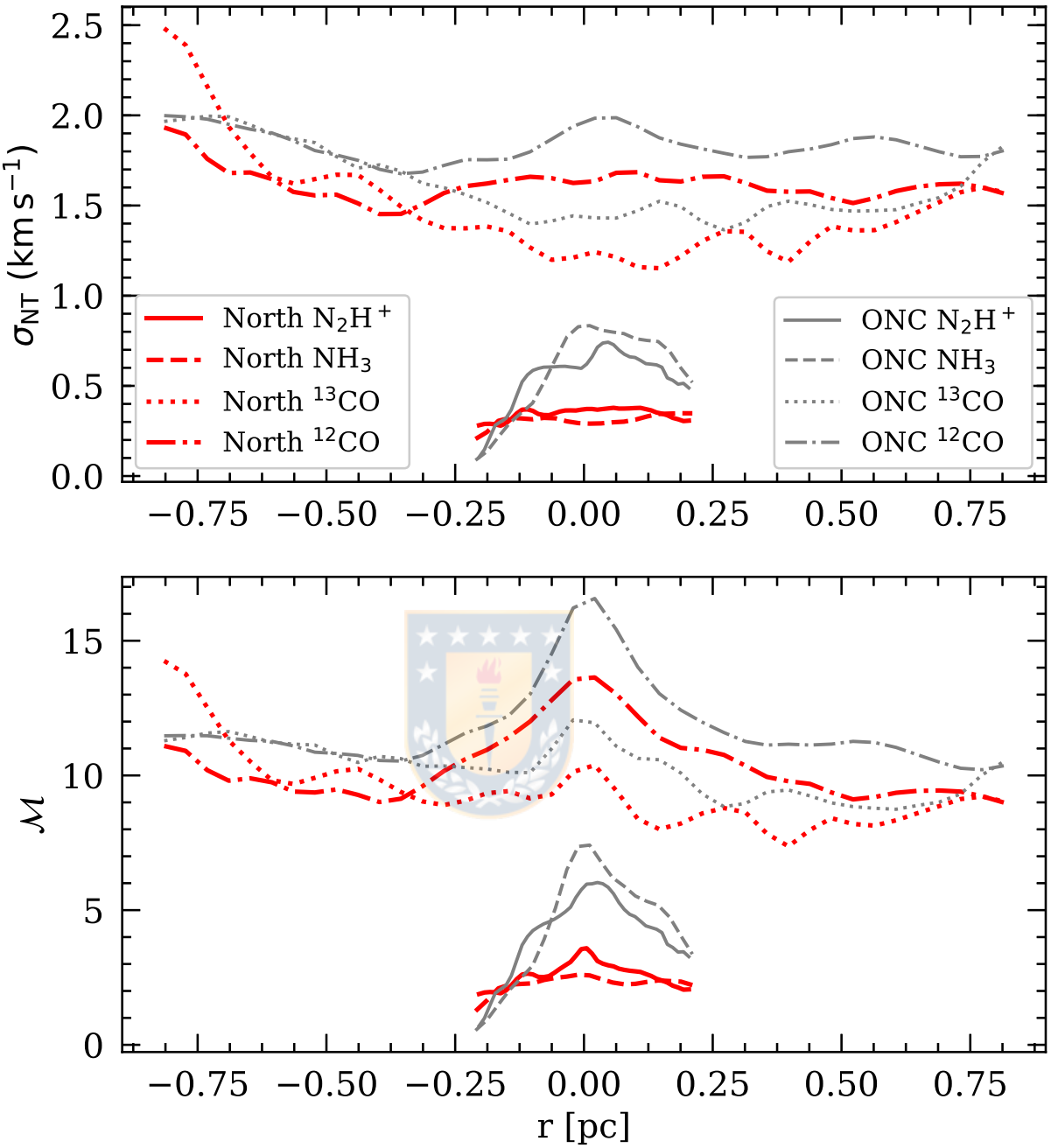

Figure 5.1: *Top:* Non-thermal component of the velocity dispersion as a function of projected radius for all tracers. ^{12}CO is the dash-dotted line, ^{13}CO is the dotted line, NH_3 is the dashed line and N_2H^+ is the solid line. The red curves represent the northern region of the ISF (from $\delta = -4.9°$ to $\delta = -5.25°$) and the gray curves represent the OMC1 region from ($\delta = -5.25°$ to $\delta = -5.48°$). *Bottom:* Mach number as a function of projected radius for the curves shown above, assuming the temperature profile from Reissl et al. (2018). The same colors of the top pannel are used.

kinetic temperature $T_{\rm k}$ to be equal to the dust temperature $T_{\rm d}$ and use the dust temperature radial profile of the ISF from the radiative transfer model presented in Reissl et al. (2018). The Reissl et al. (2018) dust temperature profile is approximated by a power-law of the form $T_d(r/pc) = 9(r/pc)^{0.22}$ K. For each tracer, the non-thermal linewidth profile is averaged in δ over the two regions considered, applying a smoothing of one beam.

The velocity dispersion profiles are shown in the top panel of Figure 5.1. The principal difference in these profiles is between different tracers (with different critical densities) rather than between regions. The velocity dispersion of all tracers tend to be higher in the ONC region (gray curves) than in the northern ISF region (red curves). The average velocity dispersion in the northern ISF region (shown in red) varies from $\bar{\sigma}_{\rm NT} = 0.25$ in NH_3 to $\bar{\sigma}_{\rm NT} = 1.61$ in ^{12}CO. This indicates that the denser gas (as traced by NH_3 and N_2H^+) is kinematically colder than the lower density gas (^{12}CO and ^{13}CO) by a factor of ~ 6. This indicates that the velocity dispersion profiles of e.g., CO alone will overestimate the dense gas line widths by factors of up to ~ 6, leading to an overestimate of the non-thermal support on the dense regions where the protostars are forming (e.g., Stutz and Gould, 2016).

The Mach number radial profiles are shown in the bottom panel of Figure 5.1. The Mach number, $\mathcal{M} = \sigma_{\rm NT}/c_s$, is the ratio between the nonthermal component of the radial velocity dispersion and the sound speed $c_s = \sqrt{\frac{kT_k}{\mu m_H}}$, where $\mu = 2.33$ is the mean molecular weight. The $\mathcal{M}$ profiles are higher in the cluster region (gray) than in the northern region (red) of the filament. The profiles show that the Mach numbers for all tracers have a tendency to rise towards the center of the filament. The decrease in temperature toward the center of the ISF (Reissl et al., 2018) drives the increase of $\mathcal{M}$ towards the center. The variation of σ_{NT} also contributes to the overall increase of $\mathcal{M}$ towards the center. The values of the Mach number show that most of the filament is above sonic ($\mathcal{M} \sim 5 - 15$). The profiles also show that the higher density tracers (NH_3, N_2H^+) are kinematically colder than the lower density gas (^{12}CO, ^{13}CO), as expected. These profiles can be compared to simulations when the simulations capture the high-mass regime of the ISF. For a low line-mass filament example see e.g., Federrath (2016), in particular their Figure 5.

We compare the specific kinetic energy in the non-thermal linewidth profiles ($K = \frac{1}{2}\sigma^2_{\rm NT}$) to the gravitational potential energy of the ISF and ONC in Figure 5.2. The gravitational potential profiles of the gas in the ISF as a whole (Stutz and Gould, 2016) and in the somewhat denser ONC region (Stutz, 2018) were derived from the *Herschel* column density data are given by:

$$\text{ISF}: \ \Phi(\text{R}) = 6.3(\text{km s}^{-1})^2 \left(\frac{\text{R}}{\text{pc}}\right)^{3/8}; \tag{5.1}$$

$$\text{ONC}: \ \Phi(\text{R}) = 27.6(\text{km s}^{-1})^2 \left(\frac{\text{R}}{\text{pc}}\right)^{0.225}. \tag{5.2}$$

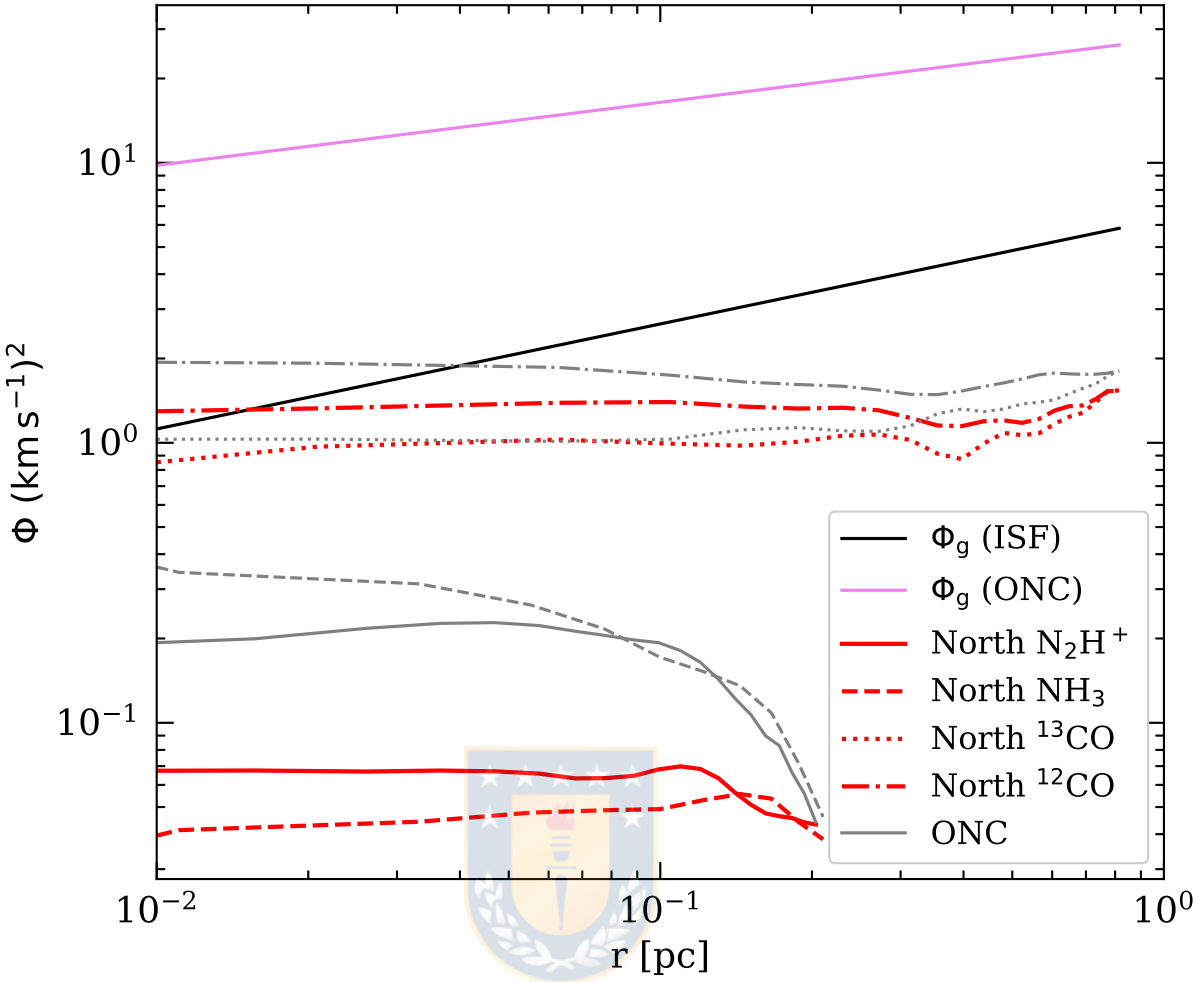

Figure 5.2: Potential as a function of radius. The black solid line represents the gravitational potential as a function of projected radius of the ISF (ONC) from Stutz and Gould (2016) (Stutz, 2018). The grey and red curves represent the specific kinetic energy from turbulence given by $\frac{1}{2}\sigma_{NT}^2$. These profiles are obtained by averaging both sides of the filament of the northern (red) and the ONC (gray) regions of the ISF.

Figure 5.2 shows that the gravitational potential profile dominates almost everywhere over the specific kinetic energy implied by the non-thermal linewidth profiles. The only exception to this is a small r region near the center of the filament; Figure 5.2 shows that the turbulent potential from the low density gas, traced by ^{12}CO and ^{13}CO, is comparable to the gravitational potential in the central region of the filament (within an enclosed radius of ~ 0.04 pc).

It is tempting to relate these non-thermal linewidth profiles to turbulent motions. However, because the linewidths contain both coherent (see below) and sub-beam motions, as observed in Kong et al. (2018) and Hacar et al. (2018) in higher resolution data, this interpretation remains problematic. Nevertheless, regardless of the specific interpretation of the linewidth profiles, these diagrams demonstrate that the the gravitational potential dominates over the kinetic energy in

the filament, showing that the filament is gravitationally bound while appearing supersonic.

5.3 Velocity ridgelines

We aim to characterize the global kinematics of the ISF in a simple fashion. For this we study the velocity ridgelines of each tracer. These provide information about the global velocity structure of the ISF. Because of the comparatively low emission levels of both NH_3 and N_2H^+, apparent in Figure 4.2, we focus on the northern ($\delta \geq -5.5\,\mathrm{deg}$) region of the ISF where detection in all four tracers are sufficiently robust to derive velocity ridgelines. To obtain the velocity ridgeline we follow the method described in Stutz and Gould (2016). We produce PV diagrams by integrating the data cube along the α axis. This way we create a projected view of the $\delta - v_{\mathrm{LSR}}$ plane. This is accomplished by excluding areas at large impact parameters from the filament ridgeline, as described above. At each δ, we record the velocity corresponding the maximum intensity. To suppress noise we apply smoothing of two beamsizes to the ridgeline for each tracer.

Figure 5.3 shows the velocity ridgelines of the four tracers (left panel) and the difference relative to the N_2H^+ velocity ridgeline (right panel). The figure shows that the four tracers have very similar ridgelines along the filament, except in the ONC region. The velocity ridgelines of all tracers present a north to south velocity gradient from $\sim 11\,\mathrm{km\,s^{-1}}$ to $\sim 9-7\,\mathrm{km\,s^{-1}}$, similar to the wave-like pattern shown in Stutz et al. (2018b). In the ONC the velocity ridgelines are more blue-shifted ($v_{\mathrm{LSR}} \sim 8\,\mathrm{km\,s^{-1}}$) than in the north, also seen in Figure 4.2. Moreover, as also seen in Figure 4.2, NH_3 follows N_2H^+ closely along the northern portion of the ISF. In the center of the ONC (near $\delta \sim -5.4°$) we observe larger differences between the ridgelines, which we interpret as velocity differences as a function of density in the more extreme central environment of the cluster.

The velocity gradients and morphologies are very similar to the ones presented in Kong et al. (2018), see Figure 2.13. Kong et al. (2018) observe the cloud at higher resolution ($8''$) using ^{12}CO, ^{13}CO, and C^{18}O (1-0). Despite the differences in resolutions and tracers, the overall morphology is similar to our ridgelines (see also Figure 1 of Hacar et al. 2017). Moreover, in a similar analysis Wu et al. (2018) showed similar fluctuations and offsets between ^{12}CO (2-1) and N_2H^+ in their velocity ridgelines of the ISF. They propose that these fluctuations may be originated from the oscillation of the filament from the slingshot mechanism (Stutz and Gould, 2016; Stutz et al., 2018b). In contrast to the Wu et al. (2018) analysis, we used the N_2H^+ velocity as reference in the right panel of Figure 5.3, as N_2H^+ traces higher density and is morelikely to provide the velocity relative to the bottom of the filament potential (as apposed to ^{12}CO; Wu et al. 2018). Neverthless, the magnitude of the fluctuations between ^{12}CO and N_2H^+ are consistent along the ISF ($\Delta \mathrm{v} \sim 1-2\,\mathrm{km\,s^{-1}}$) in both works. Wu et al. (2018) also found a $0.7\,\mathrm{km\,s^{-1}\,pc^{-1}}$ velocity gradient along the filament in the center of ONC which the propose may arise from the global contraction of the ISF, also discussed in Hacar et al. (2017).

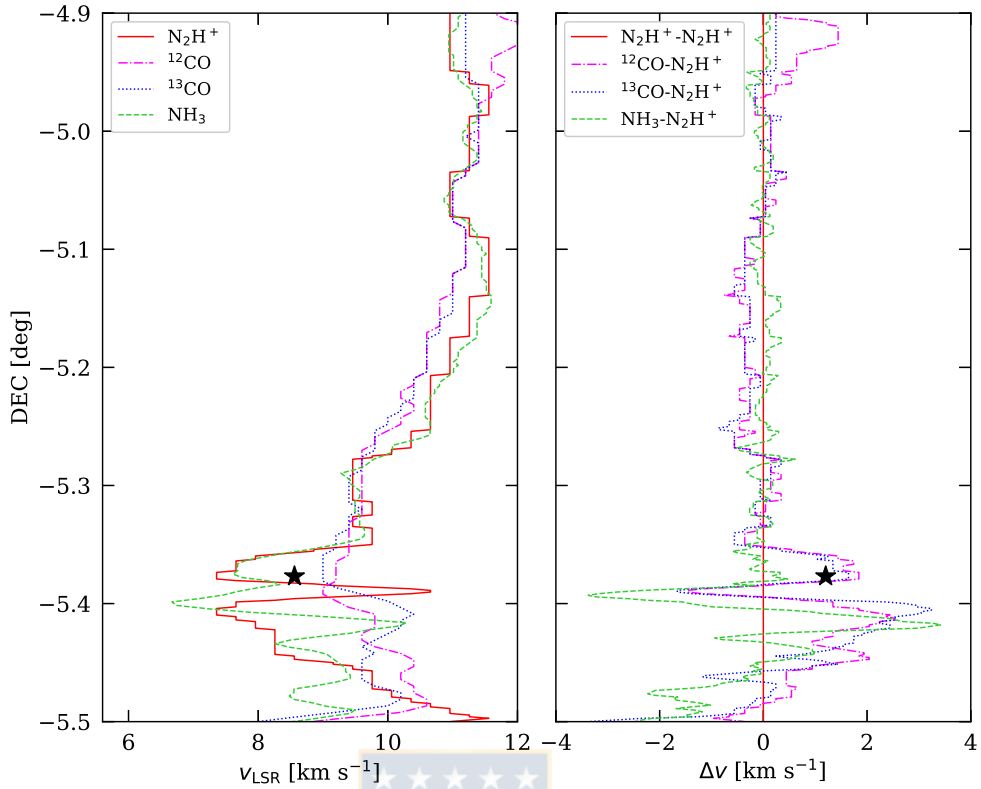

Figure 5.3: *Left*: Velocity ridgelines of the four tracers. The ridgeline is obtained from integrating the cube over the α axis. Then we computed the ridgeline as the maximum intensity value at each Declination. *Right*: Velocity ridgeline offsets of the four tracers with respect to the N_2H^+ velocity ridgeline. The dot-dashed magenta curve represents ^{12}CO, the dotted blue curve represents ^{13}CO, the dashed green curve represents NH_3 and the red solid curve represents N_2H^+.

5.4 Rotation of the filament

The ^{12}CO panel of Figure 4.2 shows a double velocity component in the northern region of the ISF. The morphology is similar to that of a tuning fork, that is, two vertical loci in velocity that merge into a single velocity near the center of the ONC. We further investigate this signature generating a PV diagram that covers the full range in α of the ^{12}CO emission of the ISF, shown in Figure 5.4. These figures show that in the northern portion of the ISF, the two main velocity components in the ^{12}CO gas are located at about $v_{LSR} \sim 6.9\,km\,s^{-1}$ and $v_{LSR} \sim 10.5\,km\,s^{-1}$, respectively, indicated with the red dashed lines. In both figures, the blueshifted component is much fainter than the redshifted one, while they seem to merge just above the ONC. As described above, in Figure 4.2 we restrict the α range of integration; meanwhile, in Figure 5.4 we include the full range in α presented in Figure 3.1. The persistence of the feature when comparing these figures indicates that the split in the northern portion of the ISF is present

over a large range of distances from the filament.

This is, to the best of our knowledge, the first place that this velocity signature and corresponding morphology has been presented. Our PV diagrams show the radial velocity stucture of the ISF in the plane of the sky. Therefore, these components can be interpreted as rotation of the filament. The presence of rotation in the ISF has been previously noted from ^{13}CO observations from Tatematsu et al. (1993), where they found a velocity gradient of $2 - 4\,\mathrm{km\,s^{-1}\,pc^{-1}}$ across the major axis of the filament. Hanawa et al. (1993) inferred an angular velocity of $\omega \sim 1 - 1.5 \times 10^{-13}\,\mathrm{s^{-1}}$ that in combination with the helical magnetic field of the ISF (Heiles, 1997) produce significant effects on the fragmentation of the filament (Hanawa et al., 1993). Schleicher and Stutz (2018) studied the MHD instabilities that arise in filaments where gravitational, magnetic and rotational energy are comparable and found that the instabilities could

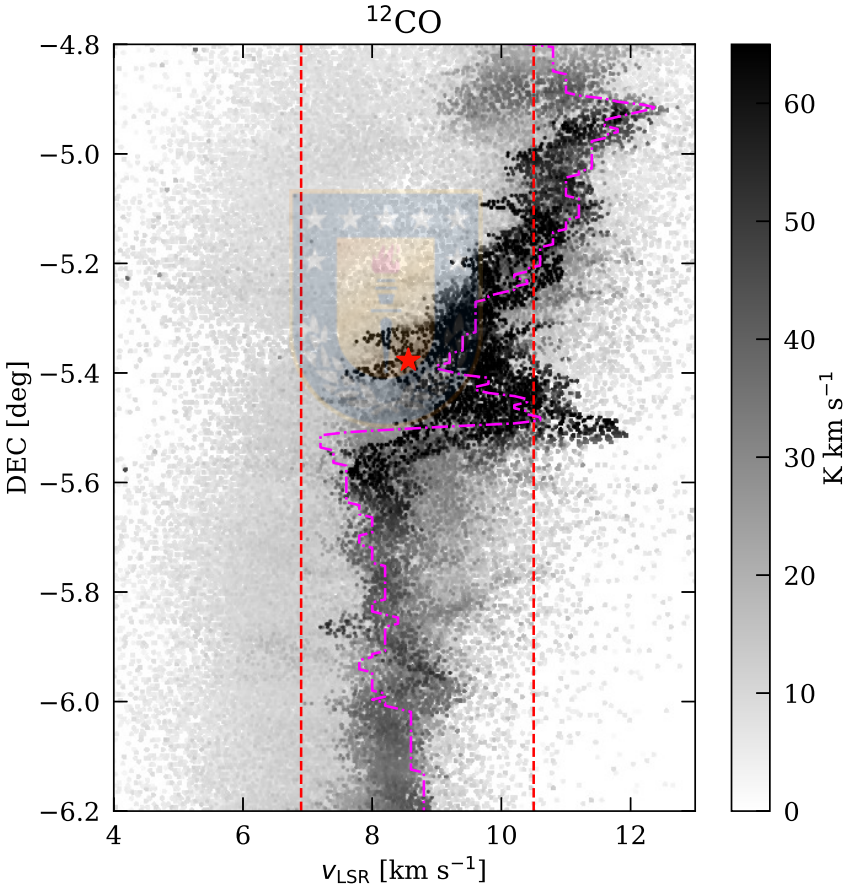

Figure 5.4: Position-velocity centroid diagram of ^{12}CO in the ISF. This map considers the full range of α values of the ^{12}CO map. The red dashed lines represent the $v_{\mathrm{LSR}} \sim 6.9\,\mathrm{km\,s^{-1}}$ and $v_{\mathrm{LSR}} \sim 10.5\,\mathrm{km\,s^{-1}}$, the velocities of the two components present in the northern region of the ISF (seen between $\delta \sim -5.2°$ and $\delta \sim -4.8°$). The star symbol indicates the position and velocity of the ONC centroid, while the dashed magenta curve indicates the velocity ridgeline of ^{12}CO presented in Figure 5.3.

give rise to the observed oscillation of the filament.

Assuming that the velocity components arise from gas rotation, we apply a simple circular velocity model to interpret this signature. We estimate the circular radius from the spatial separation of the two components and find $r = 1.3\,\mathrm{pc}$, then we compute the angular velocity as:

$$\omega = \frac{\Delta v/2}{r} = 4.5 \times 10^{-14}\,\mathrm{s}^{-1} = 1.4\,\mathrm{Myr}^{-1}. \tag{5.3}$$

This is about a factor of 3 lower than previously estimated values for the rotation of the filament (see e.g. Schleicher and Stutz, 2018, and references therein).

5.5 Velocity peaks and protostar positions

The left panel of Figure 5.5 shows the PV diagram of ^{12}CO extracted by following an area within $r = 0.8\,\mathrm{pc}$ from the dust ridgeline from Stutz (2018), in order to track the dense filament and the well of the gravitational potential. We identify six blueshifted velocity peaks from the PV diagram, indicated in Figure 5.5. Each peak is numbered and their Declination shown as horizontal lines. The peaks appear to be spaced regularly, with approximate mean separations in δ of about $\sim 0.06^\circ$ or $\sim 0.44\,\mathrm{pc}$. To investigate the possible origin of these velocity peaks, we identify their α, indicated in the right panel of Figure 5.5 with triangles. From this figure we observe that these velocity peaks are located outside of the regions with protostars and dense cores, which follow the densest regions traced by the dust ridgeline. We compare with protostar positions using the HOPS catalogue from (Stutz et al., 2013; Furlan et al., 2016), protostellar cores observed with ALMA at 3 mm continuum of the northern part of the ISF from Kainulainen et al. (2017), protostellar cores identified in the OMC1 North region observed with the Submillimeter Array (SMA) at 1.3 mm from Teixeira et al. (2016), and the outflow source in the Orion KL region from Zapata et al. (2009) observed with the SMA (see the righ panel of Figure 5.5). None of the peaks, except Peak 6 near the BN/KL region, appear to be coincident with the overlayed protostars and cores.

The peaks appear approximately periodic in the ^{12}CO PV diagram. One possible explanation for these is association with outflows from Young Stellar Objects (YSOs). Therefore, to identify possible driving sources (or lack thereof) of the regularly spaced velocity peaks, we crossmatch the velocity peaks using the SIMBAD Astronomical Database (Wenger et al., 2000), *Spitzer*/IRAC images at 3.6, 4.5, 5.8 and 8.0 μm, the HOPS catalogue from Furlan et al. (2016), the YSO catalogue from Megeath et al. (2012, 2016) and the HOPS sources associated with CO outflows in the OMC2/3 region (Kainulainen et al., 2017) to inspect the vicinity of each peak. The SIMBAD inspections are made around a circle centered at each peak with a radius of $90''$ (two ^{12}CO beams) centered on each peak. In summary, we find that Peaks 1, 3 and 6 might be associated with outflow activity in their vicinity. However, Peaks 2, 4 and 5 are not associated with any catalogued or observed YSO outflow.

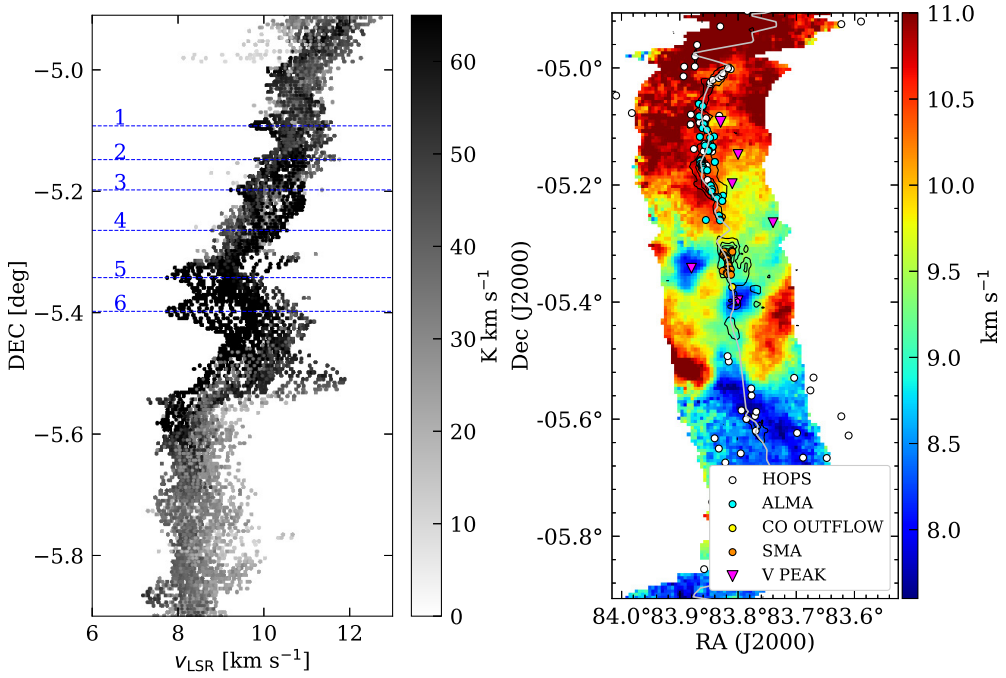

Figure 5.5: *Left*: ^{12}CO PV diagram of the region following the dust ridgeline from Stutz (2018) at a fixed projected radius of ~ 0.8 pc. *Right*: Moment 1 map of ^{12}CO showing the area that follows the dust ridgeline, where there is significant N_2H^+ emission. The velocity peaks postions in α and δ are shown with large magenta triangles. The N_2H^+ emission is indicated with black contours. The circles are point sources positions form different catalogs in the ISF: white → HOPS catalogue (Furlan et al., 2016), cyan → ALMA (Kainulainen et al., 2017), green → CO outflow in the Orion KL region (Zapata et al., 2009) and orange → protostellar cores observed with the SMA (Teixeira et al., 2016).

Another possibility for the origin of the peaks may be periodic infall into dense cores along the filament, or that the peaks are related to the wave-like nature of the ISF. The characteristic distance between the peaks is ~ 0.44 pc, while the characteristic velocity relative to the main filament velocity is $\sim 0,5\,\mathrm{km\,s^{-1}}$. These provide an estimate of the characteristic timescale of the peaks of about ~ 1 Myr, similar to the timescale for notation discussed above (Section 5.4).

Below we present a detailed discussion of the source crossmatch search for each velocity peak.

- **Peak 1**: The peak is located at R.A. = 05h35m19.2s, Decl. = $-05°05'24''$. SIMBAD inspection reveals that the closest source is an X-Ray source identified with Chandra (source I151 from Tsujimoto et al. 2002) at a separation of 12.49" from Peak 1, located at R.A. = 05h35m19.75s, Decl. = -05°05'33.4"). The second closest source is a dense core located at R.A. = 05h35m20.2s, Decl. = -05°05'14" identified with $H^{13}CO^+$ emission (Ikeda et al., 2007) at a separation of 17.98″ from Peak 1, . These two sources do not

appear to be associated with an outflow.

We identify a protostar at a separation of about $\sim 30''$ from Peak 1 in the HOPS catalog (Furlan et al., 2016). The protostar is named HOPS082 and is located at R.A. = 05h35m19.73s, Decl. = -05°04'54.6". The HOPS082 protostar is classified as a flat spectrum source, indicating that is going through the process of evolving towards a T-Tauri like disk star and is more evolved than its younger protostellar siblings. HOPS082 has a bolometric temperature of $T_{\rm BOL} = 116.4\,{\rm K}$, a bolometric luminosity of $L_{\rm BOL} = 2.4\,{\rm M}_{\odot}$ and an inner envelope mass of $M_{\rm env} = 5.5 \times 10^{-2}$ ${\rm M}_{\odot}$ (Furlan et al., 2016). We find no indication in the IRAC images from Megeath et al. (2012, 2016) of extended emission associated with possible outflow activity in this source. Given the low luminosity, low envelope mass, the evolved state and no outflow indication we discard HOPS082 as a source of the velocity feature observed in Peak 1.

On the other hand, further inspection of the SIMBAD sources around a radius of $90''$ centered on Peak 1 reveals a series of H_2 flows identified in Yu et al. (1997) that are associated with the dust condensations MMS9 (R.A. = 05h32m58.2s, Decl. = -05°07'35") and MMS10 (R.A. = 05h33m04.5s, Decl. = -05°07'34") from Chini et al. (1997). MMS9 presents a collimated east to west chain of H_2 knots that terminates 3' west of MMS9. The ^{12}CO velocity map of Orion A from Kong et al. (2018) shows in more detail the region near peak 1 and reveals an outflow structure at Decl. $\sim -5°06'$ that extends in the west to east direction. The presence of such outflows in the vicinity of Peak 1 indicate that this velocity feature could be caused by molecular outflows originating from the Chini et al. (1997) sources.

- **Peak 2**: This peak is located at R.A. = 05h35m09.6s, Decl. = -05°08'24". Inspection on the SIMBAD database shows that the closest source is a YSO located at R.A. = 05h35m10.7s, Decl. = -05°08'25.8", at a separation of $16.5''$ from Peak 2. The YSO was identified with SCUBA-2 and has a mass of 0.2342 ${\rm M}_{\odot}$ and a temperature of 10.3966 K (Salji et al., 2015). There is no evidence for outflow activity associated with this YSO. The second closest source is a pre-main sequence star located at R.A. = 05h35m10.72s, Decl. = -05°08'16.95", at a separation of 18.16" from Peak 2 identified in infrared by Jones et al. (1994). This source is detected in the Gaia catalog, indicating that it is not subject to elevated levels of extinction due to a large envelope-outflow system. This source is detected in x-rays in the Getman et al. (2017) catalog. This source is also identified in the catalog of Megeath et al. (2012, 2016) and has a steeply falling SED through the IRAC bands and exhibits no morphological indications of outflow activity in the IRAC bands. Two more YSOs from Megeath et al. (2012, 2016) appear within a radius of $90''$ from the position of Peak 2. These share similar characteristics as the YSO mentioned before, steeply falling SEDs and no morphological indications of outflow activity. Extensive Vizier and SIMBAD

inspection does not reveal any outflow near the location of Peak 2.

- **Peak 3**: The peak is located at R.A. = 05h35m12s, Decl. = -05°11'24". SIMBAD inspection shows that the closest source is separated 27.4" from Peak 3, an x-ray source (I76) located at R.A. = 05h35m10.32s , Decl. = -05°11'12.9". I76 was identified in x-ray using Chandra (Tsujimoto et al., 2002), but does not have enough information for classification. The source does not present any obvious indication of outflow activity. The second closest source is a low mass star located at R.A. = 05h35m12.7s, Decl. = -05°12'00.68", at a separation of 38.16" from Peak 3. This source was first identified in NIR by Jones et al. (1994). The star has a mass of about 0.1 $M_\odot$ (Da Rio et al., 2012). Given its evolutionary state, low mass and no apparent association to an outflow we do not regard this as a probable source of velocity Peak 3. One YSO from Megeath et al. (2012, 2016) is located at a distance of about 70" from the position of Peak 3 (R.A. = 05h35m07.52s, Decl. = $-05°11'14.14''$) and is classified as a pre-main sequence star with disk. This YSO shows no indication of outflow activity in the IRAC bands. Further SIMBAD inspection shows that this source is classified as a rapid irregular variable of the intermediate spectral type star observed in nebulosity (ISNB variable star, Samus' et al. 2017). The source is detected in the Gaia DR2 catalog. It is also identified with Chandra, is variable and was classified as a Class II protostar (Tsujimoto et al., 2002). Given the evolutionary state of this YSO and the lack of evident association to an outflow we discard this object as a source of Peak 3.

  We find three YSOs from the HOPS catalog that have been associated with CO outflows near this region (Kainulainen et al., 2017). These correspond to HOPS60 (R.A. = 05h35m23.3s, Decl. = -05°12'03.15") classified as a Class 0 protostar with a bolometric luminosity of 21.93 $L_\odot$, a bolometric temperature of 71.5 K and an envelope mass of 0.135 $M_\odot$. This YSO is associated with the FIR6b outflow from Shimajiri et al. (2009) at R.A. = 5h35m21.37s, Decl. = -5°12'05". The outflow orientation is East-West, and inspection of the position and extent reveals a very similar signature to the one present in our ^{12}CO velocity map, allowing us to conclude that Peak 3 is likely produced by the outflow associated with the FIR6 source.

- **Peak 4**: The peak is located at R.A. = 05h34m57.6s, Decl. = $-05°15'36''$. The closest source is an infrared source located at R.A. = 05h34m58.83s, Decl. = -05°15'35.7", at a separation of 18.37" from Peak 4 (Tsujimoto et al., 2003). We find no indication of outflow activity tied to this source. The second closest source is a Star located at R.A. = 05h34m56.37s, Decl. = -05°15'28.4", at a separation of 19.88" from the Peak 4. The star was first identified by Tsujimoto et al. (2003) and is also observed by 2MASS

(Cutri et al., 2003). We find no evidence of outflow activity associated to this source. We find two YSOs from Megeath et al. (2012, 2016) located at $\sim$ 45″ from Peak 4. The coordinates are R.A. = 05h34m56.67s, Decl. = -05°14'52.26" and R.A. = 05h35m00.22s, s. = -05°15'58.97" respectively. The first YSO (also identified in Gaia DR2) is classified as a pre-main sequence star with disk (Megeath et al., 2012) and also a periodic variable with a rotation period of 2.65 d (Rodríguez-Ledesma et al., 2009). The second YSO is classified as a pre-main sequence star with disk (Megeath et al., 2012) and presents variability due to rotation with a period of 1.25 d (Rodríguez-Ledesma et al., 2009). Neither of these sources show any morphological indication of outflow activity from the IRAC images.

- **Peak 5**: The peak is located at R.A. = 05h35m28.8s, Decl. = -05°20'24". SIMBAD inspection of the vicinity of the peak shows that the closest source is an infrared star at a separation of 3.7″ from Peak 5, located at R.A. = 05h35m28.8s, Decl. = -05°20'20.3" (Muench et al., 2002). This star shows no evident outflow activity. We find two YSOs from Megeath et al. (2012, 2016) located at about 45″ from Peak 5. The first YSO (at R.A. = 05h35m26.17s, Decl. = -05°20'06.04") is identified in Gaia DR2 and 2MASS. The YSO presents variability with a rotation period of 8.55 d (Rodríguez-Ledesma et al., 2009) and is classified as a pre-main sequence star with disk (Megeath et al., 2012). The second YSO (coordinates R.A. = 05h35m31.39s, Decl. = -05°20'17.05") is classified as a pre-main sequence star with disk (Megeath et al., 2012). Neither of these protostars show any morphological indication of outflow activities in the IRAC images. Given the more evolved state of the YSOs close to Peak 5 and the lack of outflow activity in the vicinity, we conclude that there is no indentified souce associated to Peak 5.

  In contrast to Peak 6 (see below), Peak 5 is most prominent in ^{12}CO, less so in ^{13}CO, and appears coincident with a dense knot in NH_3 nad N_2H^+, located just above but near the position-velocity of the ONC (see red ×-symbol in Figure 4.2).

- **Peak 6**: The peak is located at R.A. = 05h35m12s, Decl. = $-05°23'24''$. SIMBAD inspection of the vicinity of the peak reveals a crowded region with sources related to the ONC, as expected. This peak lies near the center of the cluster, in the Orion BN/KL region (Becklin and Neugebauer, 1967; Kleinmann and Low, 1967). This region is characterized by an explosion caused by the close interaction between two or more protostars about 500 yr ago (Zapata et al., 2009; Bally et al., 2017). This explosion induced a wide outflow with a scale of $\sim 1'$ that is spherically symmetric distributed around the explosion center (Bally et al., 2017). The center of the explosion is located at R.A. = 05h35m14.37s, Decl. = -05°22'27.9" (Zapata et al., 2009) at a separation of $\sim$ 79.2 from Peak 6. Taken

at face value, the postion of Peak 6 is inconsistent with the explosion from the Orion BN/KL explosion Bally et al. (2017). However, the low velocity component of the outflow (within $10\,\mathrm{km\,s^{-1}}$ from the OMC1 rest velocity $v_{\mathrm{LSR}} \sim 9\,\mathrm{km\,s^{-1}}$) appears elongated from southeast to northwest, and a $\sim$arcminute long wide blueshifted bubble that extends southeast with velocity $v_{\mathrm{LSR}} \sim 7\,\mathrm{km\,s^{-1}}$. This suggests that Peak 6 may in fact be related to the BN/KL explosion. However, in contrast to Peak 5 discussed above, the detection of Peak 6 in all tracers (see Figure 4.2), from the lower to high density gas, indicates that that interpretation of Peak 6 as driven by the BN/KL explosion may be problematic. The positon-velocity structure that we observe for Peak 6 is consistent across all tracers, which indicates that larger-scale and more global filament dynamics are responsible for shaping the observed morphology.

Chapter 6

Discussion and conclusions

The process of star formation is fundamental to understand galaxy evolution and planet formation. Most of the stars in the Galaxy are formed in massive star clusters embedded in giant molecular clouds. The Orion A molecular cloud hosts a massive dense gas structure called the Integral Shaped Filament (ISF), which in turn is forming an embedded star cluster known as the Orion Nebula Cluster (ONC). For its proximity, at a distance of $\sim$ 400 pc (e.g., Stutz et al., 2018b; Kounkel et al., 2018; Getman et al., 2019; Zucker et al., 2019), the ISF is an ideal laboratory in which to study the rapid phase of star cluster and massive star formation. In this work we used public observations of different molecular tracers from the ISF, namely ^{12}CO $(1-0)$, ^{13}CO $(1-0)$, NH_3 $(1,1)$ and N_2H^+ $(1-0)$, along with other observations, in order to characterize the velocity structure of the gas associated with the process of star cluster formation at different densities.

We present intensity-weighted PV diagrams of the four tracers mentioned in Figure 4.2. We compare these to the stellar and gas mass distribution in the region marked with the blue box in Figure 3.1. These diagrams show larger and smaller scale features in the velocity structure of the ISF.

On larger scales of the filament, we observe that the northern portion of the ISF exhibits an increasing velocity gradient from North to South, over an extent of $\sim$ 3.5 pc, terminating in the prominent blue-shifted peak detected in the four tracers at around $\sim 7\,\mathrm{km\,s^{-1}}$. This blue peak is detected over the large range of critical densities traced (see Chapter 3). The velocity gradient observed has been previously proposed to originate from the wave-like behaviour of the ISF (Stutz and Gould, 2016; Stutz, 2018; Stutz et al., 2018b; Kong et al., 2018). On the other hand, Hacar et al. (2017) proposed that the morphology of the N_2H^+ $(1-0)$ velocity gradient is driven by gravitational infall into the center of the ONC.

Below this blue peak, the filament presents a prominent gap in N_2H^+ with corresponding but faint NH_3 emission. South of the gap, faint emission from the filament is observed in all tracers to have approximately constant velocity of about $\sim 8\,\mathrm{km\,s^{-1}}$ over the remaining $\sim$ 3.5 pc

of the ISF. The filament gap is filled in ^{12}CO $(1-0)$ and ^{13}CO $(1-0)$ emission, presumably from the lower density gas present in the cloud. This emission follows a gradient in velocity from $\sim$ 10 km s^{-1} to $\sim$ 8 km s^{-1} (North to South) over the $\sim$ 0.7 pc extent of the gap. In the same δ range of the gap-filling emission, we detect a fainter but prominent redshifted peak in ^{13}CO, and a corresponding and more prominent ^{12}CO $(1-0)$ peak with velocity $\sim$ 12 km s^{-1}. The lack of N_2H^+ and NH_3 emission in the gap is consistent with the low column density and observed break in the filament ridgeline from the *Herschel* data in Stutz and Kainulainen (2015); Stutz and Gould (2016).

The northern portion of the ISF is robustly detected in the four tracers and so can be compared. Figure 4.2 shows that all tracers have similar PV morphologies over this region. We extract velocity ridgelines as a function of δ in the four tracers by integrating over the α axis, following the method described in Stutz and Gould (2016). We use the same range of α values considered for the intensity-weighted PV diagrams and compare the resulting ridgelines in Figure 5.3. We find that North of the ONC, the velocity ridgelines agree within $\sim$ 0.5 km s^{-1} between each other. However, in the ONC region we observe significant deviations. These differences can reach up to $\sim$ 3.5 km s^{-1}, highlighting large variations in velocity as a function of density. In the ONC conditions are more extreme, the lower density tracers capture elevated velocities due to the destructive nature of the propagating wave, outflows and other activity (see below). The agreement in the northern region of the ISF shows that both high and low density tracers are able to capture the main velocity component of filaments and clouds when in the absence of perturbations associated with cluster formation.

We analyze the linewidths of the four tracers in Figure 5.1 and 5.2. We find that over the northern portion of the ISF the linewidths strongly depend on the tracer, that is, the higher density gas (NH_3, N_2H^+) is kinematically colder than the lower density gas (^{12}CO, ^{13}CO). Both ^{12}CO and ^{13}CO present larger linewidths, larger Mach numbers and larger specific kinetic energy profiles than N_2H^+ and NH_3. By comparing the specific kinetic energy inferred from the linewidth profiles to the gravitational potential of the cloud from Stutz and Gould (2016); Stutz (2018), assuming cylindrical geometry in the filament, we show in Figure 5.2 that in both the ONC and the northern portion of the ISF the gas linewidths are much lower than the gravitational potential. The only exception is a small region of the ONC close to the filament ridgeline (enclosing projected radius of $\sim$ 0.04 pc), where the ^{12}CO linewidths appear in excess of the gravitational potential. However, as described above, the ^{12}CO line profile may be contaminated with elevated velocities driven by various sources, such as outflows and line of sight confusion. The specific kinetic energy profiles are relatively constant with enclosed radius, meanwhile the enclosed mass increases more steeply as a power-law and so the gravitational potential follows the same behaviour.

The radial profiles shown Figure 5.2 are consistent with the Stutz and Gould (2016) hypotesis

that the cloud is deeply bound. Stutz and Gould (2016) analyzed the stellar radial velocity distributions in the framework of the gravitational potential of the gas. Here we show that the ISF velocities are insufficient to unbind the cloud, under the assumption of cylindrical geometry and the temperature profile of the gas from Reissl et al. (2018). Our linewidth profiles capture all cloud velocities at a given projected radius from the filament. However, line of sight confusion will mostly increase the linewidths. This causes an overestimation of the inferred kinetic energies and makes them even lower than gravitational potential of the cloud. Moreover, sub-bream coherent gas motions will also contribute to the increase in the measured linewidths (e.g., Hacar et al., 2018). The fact that the cloud is gravitationally bound implies that either the cloud is undergoing gravitational collapse or that other forces, such as magnetic fields and rotation, provide the necessary support to reproduce the observed star formation efficiency.

The velocity dispersion of filaments has been characterized in simulated low mass clouds in Federrath (2016). Federrath (2016) present in their Figure 5 the Mach number radial profiles of the resulting filaments from their model with gravity, turbulence, magnetic fields and stellar feedback (shown in panel (f) of Figure 2.6). Federrath (2016) studies the velocity dispersion in the framework of the linewidth size relationship present in supersonic molecular clouds (Federrath, 2013). The profiles of Federrath (2016) show little resemblance to our observed profiles, in part due to the lower mass regime probed in their simulations (total cloud mass of $M = 388\,\mathrm{M}_{\odot}$). We find that our Mach numbers are larger and increase towards the center of the filament for all tracers. One may argue that our observed profiles suffer from various types of contamination, such as star formation and e.g., associated outflows; however, the principal difference that must be addressed first in order to understand this discrepancy is the mass the simulations, which must be carried at larger masses (and mass per unit length values) in order to characterize systems like the ISF.

We show in Figure 5.4 the ^{12}CO intensity-weighted PV diagram extracted over the full range of α in this dataset. We highlight the large scale structure seen in the northern region of the ISF. In particular, we find two velocity components in the North, which they appear to merge at the ONC (indicated with a red star in Figure 5.4). The first component is faint and is detected along the entire length of the ISF and the second component is the main velocity gradient discussed above. These two components can be interpreted as a signature of rotation, with an associated timescale of the angular velocity of $\sim 1.4\,\mathrm{Myr}^{-1}$. However, their relation to the overall large-scale wave-like velocity structure is not presently understood.

On small scales, we highlight three prominent aspects of our analysis.

In Figure 4.2 the peak of the mass distribution of the stars and gas, interpreted as the center of gravitational infall, is offset from the prominent blue-shifted velocity peak seen in N_2H^+ at $\delta = -5.4°$. Moreover, in Figure 4.2 we plot the mean systemic velocity and the center of mass of

the ONC with a red ×-symbol, showing that the ONC is offset both in velocity and δ from the velocity peaks in all tracers. Our interpretation of this is that gravitational collapse alone is not a cause of this offset; this offset requires the action of other forces to shape the filament, namely the possible action of the magnetic field (Stutz and Gould, 2016). We also note from Figure 4.2 that the velocity of the peak depends on the tracer: we find values of $7.8, 7.3, 6.4, 6.4\,\mathrm{km\,s^{-1}}$ for ^{12}CO, ^{13}CO, NH_3, and N_2H^+, respectively. That is, we observe a shift in the velocity of the blue peak such that both the N_2H^+ and NH_3 velocities are more blue-shifted compared to ^{12}CO and ^{13}CO and to the cloud systemic velocities. This indicates that on small scales the gas at different densitites in the ONC moves at different velocities, a property also seen in Figure 5.3, such that the N_2H^+ and NH_3 gas appear more blue-shifted relative to their lower density counterparts.

Another small scale feature observed in Figure 4.2 are the twistings and turnings present in the NH_3 and N_2H^+ PV diagrams along the northern portion of the ISF. These structures are robustly replicated in both tracers, which were acquired and analyzed independently, indicating that these structures are real. These structures appear as a small-scale wave, also observed in the Kong et al. (2018) PV diagrams (see Figure 2.13 for the case of ^{13}CO). While N_2H^+ shows approximately vertical structures, reflecting short timescales, the lower density NH_3 appears to have more complex structure where the oscillations in radial velocity appear more pronounced. The PV structures give the impression of wrapping around the main axis of the ISF, like a torsional wave would behave. The nature of these structures and their relation with the larger scale wave is not presently understood.

In Figure 5.5 we observe the presence of 6 regularly spaced ($\sim 0.44\,\mathrm{pc}$ in projection) ^{12}CO velocity peaks along the northern portion of the ISF (see Section 5.5). We identify the location of these peaks from the CO PV diagram (Figure 5.5) and compare with the position of nearby protostellar sources. None of the peaks, except the main blue-shifted velocity peak near the center of the ONC, appear coincident with known protostellar sources, but 2 out of 6 might still be associated with nearby YSO outflows (see text). For the remaining 3 peaks, we fail to find any obvious protostellar association, so the origin of these peaks remains unexplained. One possibility is periodic infall into dense cores in the filament, another possibility is that the peaks are related to the wave-like appearance nature of the filament. The characteristic timescale of these peaks is $\sim 1\,\mathrm{Myr}$, similar to the rotation timescale discussed above. Suggesting that the wave-like nature of the ISF may connect the timescales between small and large scale phenomena.

The analysis presented here suggests a global view of cluster formation in massive filaments that is more complex than previously suggested. We detect large and smaller scale kinematic features that need explanation. We suggest that, as previously proposed, the action of magnetic fields impacts the kinematic appearance of the ISF. Specifically, the different properties seen in the northern portion of the filament compared to the southern one.

Bibliography

J. F. Alves, C. J. Lada, and E. A. Lada. Internal structure of a cold dark molecular cloud inferred from the extinction of background starlight. *Nature*, 409:159–161, January 2001.

J. Bally, W. D. Langer, A. A. Stark, and R. W. Wilson. Filamentary structure in the Orion molecular cloud. *ApJL*, 312:L45–L49, January 1987. doi: 10.1086/184817.

J. Bally, A. Ginsburg, H. Arce, J. Eisner, A. Youngblood, L. Zapata, and H. Zinnecker. The ALMA View of the OMC1 Explosion in Orion. *ApJ*, 837:60, March 2017. doi: 10.3847/1538-4357/aa5c8b.

Nate Bastian, Kevin R. Covey, and Michael R. Meyer. A Universal Stellar Initial Mass Function? A Critical Look at Variations. *ARA&A*, 48:339–389, Sep 2010. doi: 10.1146/annurev-astro-082708-101642.

E. E. Becklin and G. Neugebauer. Observations of an Infrared Star in the Orion Nebula. *ApJ*, 147:799, February 1967. doi: 10.1086/149055.

T. C. N. Boekholt, A. M. Stutz, M. Fellhauer, D. R. G. Schleicher, and D. R. Matus Carrillo. Dynamical ejections of stars due to an accelerating gas filament. *MNRAS*, 471:3590–3598, November 2017. doi: 10.1093/mnras/stx1821.

R. Chini, B. Reipurth, D. Ward-Thompson, J. Bally, L.-Å. Nyman, A. Sievers, and Y. Billawala. Dust Filaments and Star Formation in OMC-2 and OMC-3. *ApJL*, 474:L135–L138, January 1997. doi: 10.1086/310436.

Richard M. Crutcher. Magnetic Fields in Molecular Clouds: Observations Confront Theory. *ApJ*, 520(2):706–713, Aug 1999. doi: 10.1086/307483.

Richard M. Crutcher. Magnetic Fields in Molecular Clouds. *ARA&A*, 50:29–63, Sep 2012. doi: 10.1146/annurev-astro-081811-125514.

R. M. Cutri, M. F. Skrutskie, S. van Dyk, C. A. Beichman, J. M. Carpenter, T. Chester, L. Cambresy, T. Evans, J. Fowler, J. Gizis, E. Howard, J. Huchra, T. Jarrett, E. L. Kopan, J. D. Kirkpatrick, R. M. Light, K. A. Marsh, H. McCallon, S. Schneider, R. Stiening, M. Sykes,

M. Weinberg, W. A. Wheaton, S. Wheelock, and N. Zacarias. VizieR Online Data Catalog: 2MASS All-Sky Catalog of Point Sources (Cutri+ 2003). *VizieR Online Data Catalog*, art. II/246, Jun 2003.

N. Da Rio, M. Robberto, L. A. Hillenbrand, T. Henning, and K. G. Stassun. The Initial Mass Function of the Orion Nebula Cluster across the H-burning Limit. *ApJ*, 748:14, March 2012. doi: 10.1088/0004-637X/748/1/14.

F. Daniel, M.-L. Dubernet, M. Meuwly, J. Cernicharo, and L. Pagani. Collisional excitation rate coefficients of N_2H^+ by He. *MNRAS*, 363:1083–1091, November 2005. doi: 10.1111/j.1365-2966.2005.09542.x.

Guido De Marchi, Francesco Paresce, and Simon Portegies Zwart. The Stellar IMF of Galactic Clusters and Its Evolution. In E. Corbelli, F. Palla, and H. Zinnecker, editors, *The Initial Mass Function 50 Years Later*, volume 327 of *Astrophysics and Space Science Library*, page 77, Jan 2005. doi: 10.1007/978-1-4020-3407-7_11.

II Evans, Neal J. Physical Conditions in Regions of Star Formation. *ARA&A*, 37:311–362, Jan 1999. doi: 10.1146/annurev.astro.37.1.311.

C. Federrath. On the universality of interstellar filaments: theory meets simulations and observations. *MNRAS*, 457:375–388, March 2016. doi: 10.1093/mnras/stv2880.

C. Federrath and R. S. Klessen. The Star Formation Rate of Turbulent Magnetized Clouds: Comparing Theory, Simulations, and Observations. *ApJ*, 761:156, December 2012. doi: 10.1088/0004-637X/761/2/156.

Christoph Federrath. On the universality of supersonic turbulence. *MNRAS*, 436(2):1245–1257, Dec 2013. doi: 10.1093/mnras/stt1644.

R. K. Friesen, J. E. Pineda, co-PIs, E. Rosolowsky, F. Alves, A. Chacón-Tanarro, H. How-Huan Chen, M. Chun-Yuan Chen, J. Di Francesco, J. Keown, H. Kirk, A. Punanova, Y. Seo, Y. Shirley, A. Ginsburg, C. Hall, S. S. R. Offner, A. Singh, H. G. Arce, P. Caselli, A. A. Goodman, P. G. Martin, C. Matzner, P. C. Myers, E. Redaelli, and GAS Collaboration. The Green Bank Ammonia Survey: First Results of NH_3 Mapping of the Gould Belt. *ApJ*, 843:63, July 2017. doi: 10.3847/1538-4357/aa6d58.

E. Furlan, W. J. Fischer, B. Ali, A. M. Stutz, T. Stanke, J. J. Tobin, S. T. Megeath, M. Osorio, L. Hartmann, N. Calvet, C. A. Poteet, J. Booker, P. Manoj, D. M. Watson, and L. Allen. The Herschel Orion Protostar Survey: Spectral Energy Distributions and Fits Using a Grid of Protostellar Models. *ApJS*, 224:5, May 2016. doi: 10.3847/0067-0049/224/1/5.

K. V. Getman, P. S. Broos, M. A. Kuhn, E. D. Feigelson, A. J. W. Richert, Y. Ota, M. R. Bate, and G. P. Garmire. Star Formation In Nearby Clouds (SFiNCs): X-Ray and Infrared Source Catalogs and Membership. *ApJS*, 229:28, April 2017. doi: 10.3847/1538-4365/229/2/28.

K. V. Getman, E. D. Feigelson, M. A. Kuhn, and G. P. Garmire. Gaia Stellar Kinematics in the Head of the Orion A Cloud: Runaway Stellar Groups and Gravitational Infall. *arXiv e-prints*, art. arXiv:1905.10251, May 2019.

A. Ginsburg and J. Mirocha. PySpecKit: Python Spectroscopic Toolkit. Astrophysics Source Code Library, September 2011.

A. Ginsburg, T. Robitaille, C. Beaumont, E. Rosolowsky, A. Leroy, C. Brogan, T. Hunter, P. Teuben, and D. Brisbin. Radio Astronomy Tools in Python: Spectral-cube, pvextractor, and more. In D. Iono, K. Tatematsu, A. Wootten, and L. Testi, editors, *Revolution in Astronomy with ALMA: The Third Year*, volume 499 of *Astronomical Society of the Pacific Conference Series*, pages 363–364, Dec 2015.

A. Hacar, J. Alves, M. Tafalla, and J. R. Goicoechea. Gravitational collapse of the OMC-1 region. *arXiv*, 602:L2, June 2017. doi: 10.1051/0004-6361/201730732.

A. Hacar, M. Tafalla, J. Forbrich, J. Alves, S. Meingast, J. Grossschedl, and P. S. Teixeira. An ALMA study of the Orion Integral Filament. I. Evidence for narrow fibers in a massive cloud. *arXiv*, 610:A77, March 2018. doi: 10.1051/0004-6361/201731894.

Tomoyuki Hanawa, Fumitaka Nakamura, Tomoaki Matsumoto, Takenori Nakano, Ken'ichi Tatematsu, Tomofumi Umemoto, Osamu Kameya, Naomi Hirano, Tetsuo Hasegawa, and Norio Kaifu. Effects of Magnetic Fields and Rotation on the Fragmentation of Filamentary Molecular Clouds: Comparison of the Theory with the Orion A Cloud. *ApJ*, 404:L83, Feb 1993. doi: 10.1086/186749.

C. Heiles. A Holistic View of the Magnetic Field in the Eridanus/Orion Region. *ApJS*, 111: 245–288, July 1997. doi: 10.1086/313010.

M. Hennemann, F. Motte, N. Schneider, P. Didelon, T. Hill, D. Arzoumanian, S. Bontemps, T. Csengeri, Ph. André, V. Konyves, F. Louvet, A. Marston, A. Men'shchikov, V. Minier, Q. Nguyen Luong, P. Palmeirim, N. Peretto, M. Sauvage, A. Zavagno, L. D. Anderson, J. Ph. Bernard, J. Di Francesco, D. Elia, J. Z. Li, P. G. Martin, S. Molinari, S. Pezzuto, D. Russeil, K. L. J. Rygl, E. Schisano, L. Spinoglio, T. Sousbie, D. Ward-Thompson, and G. J. White. The spine of the swan: a Herschel study of the DR21 ridge and filaments in Cygnus X. *arXiv*, 543:L3, Jul 2012. doi: 10.1051/0004-6361/201219429.

A. K. Hernandez and J. C. Tan. The Dynamical State of Filamentary Infrared Dark Clouds. *ApJ*, 730:44, March 2011. doi: 10.1088/0004-637X/730/1/44.

N. Ikeda, K. Sunada, and Y. Kitamura. A Survey of Dense Cores in the Orion A Cloud. *ApJ*, 665:1194–1219, August 2007. doi: 10.1086/519484.

T. J. Jones, J. Mergen, S. Odewahn, R. D. Gehrz, I. Gatley, K. M. Merrill, R. Probst, and C. E. Woodward. A near-infrared survey of the OMC2 region. *AJ*, 107:2120–2130, June 1994. doi: 10.1086/117023.

J. Kainulainen, A. M. Stutz, T. Stanke, J. Abreu-Vicente, H. Beuther, T. Henning, K. G. Johnston, and S. T. Megeath. Resolving the fragmentation of high line-mass filaments with ALMA: the integral shaped filament in Orion A. *arXiv*, 600:A141, April 2017. doi: 10.1051/0004-6361/201628481.

Jr. Kennicutt, Robert C. The Global Schmidt Law in Star-forming Galaxies. *ApJ*, 498(2): 541–552, May 1998. doi: 10.1086/305588.

Robert C. Kennicutt and Neal J. Evans. Star Formation in the Milky Way and Nearby Galaxies. *ARA&A*, 50:531–608, Sep 2012. doi: 10.1146/annurev-astro-081811-125610.

D. E. Kleinmann and F. J. Low. Discovery of an Infrared Nebula in Orion. *ApJL*, 149:L1, July 1967. doi: 10.1086/180039.

S. Kong, H. G. Arce, J. R. Feddersen, J. M. Carpenter, F. Nakamura, Y. Shimajiri, A. Isella, V. Ossenkopf-Okada, A. I. Sargent, Á. Sánchez-Monge, S. T. Suri, J. Kauffmann, T. Pillai, J. E. Pineda, J. Koda, J. Bally, D. C. Lis, P. Padoan, R. Klessen, S. Mairs, A. Goodman, P. Goldsmith, P. McGehee, P. Schilke, P. J. Teuben, M. José Maureira, C. Hara, A. Ginsburg, B. Burkhart, R. J. Smith, A. Schmiedeke, J. L. Pineda, S. Ishii, K. Sasaki, R. Kawabe, Y. Urasawa, S. Oyamada, and Y. Tanabe. The CARMA-NRO Orion Survey. *ApJS*, 236:25, June 2018. doi: 10.3847/1538-4365/aabafc.

Marina Kounkel, Kevin Covey, Genaro Suárez, Carlos Román-Zúñiga, Jesus Hernandez, Keivan Stassun, Karl O. Jaehnig, Eric D. Feigelson, Karla Peña Ramírez, Alexandre Roman-Lopes, Nicola Da Rio, Guy S. Stringfellow, J. Serena Kim, Jura Borissova, José G. Fernández-Trincado, Adam Burgasser, D. A. García-Hernández, Olga Zamora, Kaike Pan, and Christian Nitschelm. The APOGEE-2 Survey of the Orion Star-forming Complex. II. Six-dimensional Structure. *AJ*, 156(3):84, Sep 2018. doi: 10.3847/1538-3881/aad1f1.

P. Kroupa. On the variation of the initial mass function. *MNRAS*, 322:231–246, April 2001. doi: 10.1046/j.1365-8711.2001.04022.x.

P. Kroupa, T. Jeřábková, F. Dinnbier, G. Beccari, and Z. Yan. Evidence for feedback and stellar-dynamically regulated bursty star cluster formation: the case of the Orion Nebula Cluster. *arXiv*, 612:A74, April 2018. doi: 10.1051/0004-6361/201732151.

M. R. Krumholz, M. R. Bate, H. G. Arce, J. E. Dale, R. Gutermuth, R. I. Klein, Z. Y. Li, F. Nakamura, and Q. Zhang. Star Cluster Formation and Feedback. In Henrik Beuther, Ralf S. Klessen, Cornelis P. Dullemond, and Thomas Henning, editors, *Protostars and Planets VI*, page 243, Jan 2014. doi: 10.2458/azu_uapress_9780816531240-ch011.

Mark R. Krumholz. Notes on Star Formation. *arXiv e-prints*, art. arXiv:1511.03457, Nov 2015.

Charles J. Lada and Elizabeth A. Lada. Embedded Clusters in Molecular Clouds. *ARA&A*, 41: 57–115, Jan 2003. doi: 10.1146/annurev.astro.41.011802.094844.

R. B. Larson. Turbulence and star formation in molecular clouds. *MNRAS*, 194:809–826, Mar 1981. doi: 10.1093/mnras/194.4.809.

Hua-bai Li, C. Darren Dowell, Alyssa Goodman, Roger Hildebrand , and Giles Novak. Anchoring Magnetic Field in Turbulent Molecular Clouds. *ApJ*, 704(2):891–897, Oct 2009. doi: 10.1088/0004-637X/704/2/891.

Hong-Li Liu, Amelia Stutz, and Jing-Hua Yuan. Large-scale periodic velocity oscillation in the filamentary cloud G350.54+0.69. *MNRAS*, page 1279, May 2019. doi: 10.1093/mnras/stz1340.

C. F. McKee and E. C. Ostriker. Theory of Star Formation. *ARA&A*, 45:565–687, September 2007. doi: 10.1146/annurev.astro.45.051806.110602.

S. T. Megeath, R. Gutermuth, J. Muzerolle, E. Kryukova, K. Flaherty, J. L. Hora, L. E. Allen, L. Hartmann, P. C. Myers, J. L. Pipher, J. Stauffer, E. T. Young, and G. G. Fazio. The Spitzer Space Telescope Survey of the Orion A and B Molecular Clouds. I. A Census of Dusty Young Stellar Objects and a Study of Their Mid-infrared Variability. *AJ*, 144:192, December 2012. doi: 10.1088/0004-6256/144/6/192.

S. T. Megeath, R. Gutermuth, J. Muzerolle, E. Kryukova, J. L. Hora, L. E. Allen, K. Flaherty, L. Hartmann, P. C. Myers, J. L. Pipher, J. Stauffer, E. T. Young, and G. G. Fazio. The Spitzer Space Telescope Survey of the Orion A and B Molecular Clouds. II. The Spatial Distribution and Demographics of Dusty Young Stellar Objects. *AJ*, 151:5, January 2016. doi: 10.3847/0004-6256/151/1/5.

F. Motte, A. Zavagno, S. Bontemps, N. Schneider, M. Hennemann, J. di Francesco, Ph. André, P. Saraceno, M. Griffin, A. Marston, D. Ward-Thompson, G. White, V. Minier, A. Men'shchikov, T. Hill, A. Abergel, L. D. Anderson, H. Aussel, Z. Balog, J. P. Baluteau, J. Ph. Bernard, P. Cox, T. Csengeri, L. Deharveng, P. Didelon, A. M. di Giorgio, P. Hargrave, M. Huang, J. Kirk, S. Leeks, J. Z. Li, P. Martin, S. Molinari, Q. Nguyen-Luong, G. Olofsson, P. Persi, N. Peretto, S. Pezzuto, H. Roussel, D. Russeil, S. Sadavoy, M. Sauvage, B. Sibthorpe,

L. Spinoglio, L. Testi, D. Teyssier, R. Vavrek, C. D. Wilson, and A. Woodcraft. Initial highlights of the HOBYS key program, the Herschel imaging survey of OB young stellar objects. *arXiv*, 518:L77, Jul 2010. doi: 10.1051/0004-6361/201014690.

F. Motte, S. Bontemps, and F. Louvet. High-Mass Star and Massive Cluster Formation in the Milky Way. *ArXiv e-prints*, May 2017.

A. A. Muench, E. A. Lada, C. J. Lada, and J. Alves. The Luminosity and Mass Function of the Trapezium Cluster: From B Stars to the Deuterium-burning Limit. *ApJ*, 573:366–393, July 2002. doi: 10.1086/340554.

C. R. O'dell. The Orion Nebula and its Associated Population. *ARA&A*, 39:99–136, Jan 2001. doi: 10.1146/annurev.astro.39.1.99.

P. Palmeirim, P. André, J. Kirk, D. Ward-Thompson, D. Arzoumanian, V. Könyves, P. Didelon, N. Schneider, M. Benedettini, S. Bontemps, J. Di Francesco, D. Elia, M. Griffin, M. Hennemann, T. Hill, P. G. Martin, A. Men'shchikov, S. Molinari, F. Motte, Q. Nguyen Luong, D. Nutter, N. Peretto, S. Pezzuto, A. Roy, K. L. J. Rygl, L. Spinoglio, and G. L. White. Herschel view of the Taurus B211/3 filament and striations: evidence of filamentary growth? *arXiv*, 550:A38, February 2013. doi: 10.1051/0004-6361/201220500.

T. Preibisch, V. Roccatagliata, B. Gaczkowski, and T. Ratzka. Herschel far-infrared observations of the Carina Nebula complex. I. Introduction and global cloud structure. *arXiv*, 541:A132, May 2012. doi: 10.1051/0004-6361/201218851.

S. Reissl, A. M. Stutz, R. Brauer, E. W. Pellegrini, D. R. G. Schleicher, and R. Klessen. Magnetic fields in star forming systems (I): Idealized synthetic signatures of dust polarization and Zeeman splitting in filaments. *ArXiv e-prints*, May 2018.

F. Ripple, M. H. Heyer, R. Gutermuth, R. L. Snell, and C. M. Brunt. CO abundance variations in the Orion Molecular Cloud. *MNRAS*, 431:1296–1313, May 2013. doi: 10.1093/mnras/stt247.

T. P. Robitaille and B. A. Whitney. The Present-Day Star Formation Rate of the Milky Way Determined from Spitzer-Detected Young Stellar Objects. *ApJL*, 710:L11–L15, February 2010. doi: 10.1088/2041-8205/710/1/L11.

M. V. Rodríguez-Ledesma, R. Mundt, and J. Eislöffel. Rotational studies in the Orion Nebula Cluster: from solar mass stars to brown dwarfs. *arXiv*, 502:883–904, August 2009. doi: 10.1051/0004-6361/200811427.

C. J. Salji, J. S. Richer, J. V. Buckle, J. Hatchell, H. Kirk, S. F. Beaulieu, D. S. Berry, H. Broekhoven-Fiene, M. J. Currie, M. Fich, T. Jenness, D. Johnstone, J. C. Mottram, D. Nutter, K. Pattle, J. E. Pineda, C. Quinn, S. Tisi, S. Walker-Smith, J. di Francesco,

M. R. Hogerheijde, D. Ward-Thompson, P. Bastien, H. Butner, M. Chen, A. Chrysostomou, S. Coude, C. J. Davis, E. Drabek-Maunder, A. Duarte-Cabral, J. Fiege, P. Friberg, R. Friesen, G. A. Fuller, S. Graves, J. Greaves, J. Gregson, W. Holland, G. Joncas, J. M. Kirk, L. B. G. Knee, S. Mairs, K. Marsh, B. C. Matthews, G. Moriarty-Schieven, J. Rawlings, D. Robertson, E. Rosolowsky, D. Rumble, S. Sadavoy, H. Thomas, N. Tothill, S. Viti, G. J. White, C. D. Wilson, J. Wouterloot, J. Yates, and M. Zhu. The JCMT Gould Belt Survey: constraints on prestellar core properties in Orion A North. *MNRAS*, 449:1769–1781, May 2015. doi: 10.1093/mnras/stu2297.

E. E. Salpeter. The Luminosity Function and Stellar Evolution. *ApJ*, 121:161, January 1955. doi: 10.1086/145971.

N. N. Samus', E. V. Kazarovets, O. V. Durlevich, N. N. Kireeva, and E. N. Pastukhova. General catalogue of variable stars: Version GCVS 5.1. *Astronomy Reports*, 61:80–88, January 2017. doi: 10.1134/S1063772917010085.

D. R. G. Schleicher and A. Stutz. Magnetic tension and instabilities in the Orion A integral-shaped filament. *MNRAS*, 475:121–127, March 2018. doi: 10.1093/mnras/stx2975.

Maarten Schmidt. The Rate of Star Formation. *ApJ*, 129:243, Mar 1959. doi: 10.1086/146614.

Y. Shimajiri, S. Takahashi, S. Takakuwa, M. Saito, and R. Kawabe. Millimeter- and Submillimeter-Wave Observations of the OMC-2/3 Region. IV Interaction between the Outflow and the Dense Gas in the Cluster Forming Region of OMC-2 FIR 6. *Publications of the Astronomical Society of Japan*, 61:1055–1063, October 2009. doi: 10.1093/pasj/61.5.1055.

Y. L. Shirley. The Critical Density and the Effective Excitation Density of Commonly Observed Molecular Dense Gas Tracers. *PASP*, 127:299, March 2015. doi: 10.1086/680342.

A. M. Stutz. Slingshot mechanism for clusters: Gas density regulates star density in the Orion Nebula Cluster (M42). *MNRAS*, 473:4890–4899, February 2018. doi: 10.1093/mnras/stx2629.

A. M. Stutz and A. Gould. Slingshot mechanism in Orion: Kinematic evidence for ejection of protostars by filaments. *arXiv*, 590:A2, May 2016. doi: 10.1051/0004-6361/201527979.

A. M. Stutz and J. Kainulainen. Evolution of column density distributions within Orion A. *arXiv*, 577:L6, May 2015. doi: 10.1051/0004-6361/201526243.

A. M. Stutz, J. J. Tobin, T. Stanke, S. T. Megeath, W. J. Fischer, T. Robitaille, T. Henning, B. Ali, J. di Francesco, E. Furlan, L. Hartmann, M. Osorio, T. L. Wilson, L. Allen, O. Krause, and P. Manoj. A Herschel and APEX Census of the Reddest Sources in Orion: Searching for the Youngest Protostars. *ApJ*, 767:36, April 2013. doi: 10.1088/0004-637X/767/1/36.

A. M. Stutz, V. I. Gonzalez-Lobos, and A. Gould. Gaia: Orion's Integral Shaped Filament is a Standing Wave. *ArXiv e-prints*, July 2018a.

Amelia M. Stutz, Valentina I. Gonzalez-Lobos, and Andrew Gould. Gaia: Orion's Integral Shaped Filament is a Standing Wave. *arXiv e-prints*, art. arXiv:1807.11496, Jul 2018b.

Jiayi Sun, Adam K. Leroy, Andreas Schruba, Erik Rosolowsky, Annie Hughes, J. M. Diederik Kruijssen, Sharon Meidt, Eva Schinnerer, Guillermo A. Blanc, Frank Bigiel, Alberto D. Bolatto, Mélanie Chevance, Brent Groves, Cinthya N. Herrera, Alexand er P. S. Hygate, Jérôme Pety, Miguel Querejeta, Antonio Usero, and Dyas Utomo. Cloud-scale Molecular Gas Properties in 15 Nearby Galaxies. *ApJ*, 860(2):172, Jun 2018. doi: 10.3847/1538-4357/aac326.

K. Tatematsu, R. Kandori, T. Umemoto, and Y. Sekimoto. N_2H^+ and HC_3N Observations of the Orion A Cloud. *Publications of the Astronomical Society of Japan*, 60:407–419, June 2008. doi: 10.1093/pasj/60.3.407.

Ken'ichi Tatematsu, Tomofumi Umemoto, Osamu Kameya, Naomi Hirano, Tetsuo Hasegawa, Masahiko Hayashi, Takahiro Iwata, Norio Kaifu, Hitomi Mikami, and Yasuhiro Murata. Molecular Cloud Cores in the Orion A Cloud. I. Nobeyama CS (1–0) Survey. *ApJ*, 404: 643, Feb 1993. doi: 10.1086/172318.

P. S. Teixeira, S. Takahashi, L. A. Zapata, and P. T. P. Ho. Two-level hierarchical fragmentation in the northern filament of the Orion Molecular Cloud 1. *arXiv*, 587:A47, March 2016. doi: 10.1051/0004-6361/201526807.

M. Tsujimoto, K. Koyama, Y. Tsuboi, M. Goto, and N. Kobayashi. X-Ray Properties of Young Stellar Objects in OMC-2 and OMC-3 from the Chandra X-Ray Observatory. *ApJ*, 566: 974–981, February 2002. doi: 10.1086/338110.

M. Tsujimoto, K. Koyama, N. Kobayashi, M. Goto, Y. Tsuboi, and A. T. Tokunaga. Deep Near-Infrared Observations and Identifications of Chandra Sources in Orion Molecular Clouds 2 and 3. *AJ*, 125:1537–1545, March 2003. doi: 10.1086/346277.

Ewine F. van Dishoeck. ISO Spectroscopy of Gas and Dust: From Molecular Clouds to Protoplanetary Disks. *ARA&A*, 42(1):119–167, Sep 2004. doi: 10.1146/annurev.astro.42.053102.134010.

M. Wenger, F. Ochsenbein, D. Egret, P. Dubois, F. Bonnarel, S. Borde, F. Genova, G. Jasniewicz, S. Laloë, S. Lesteven, and R. Monier. The SIMBAD astronomical database. The CDS reference database for astronomical objects. *A&AS*, 143:9–22, April 2000. doi: 10.1051/aas:2000332.

T. L. Wilson, K. Rohlfs, and S. Hüttemeister. *Tools of Radio Astronomy*. Springer-Verlag, 2009. doi: 10.1007/978-3-540-85122-6.

G. Wu, E. Jarken, W. Baan, J.-J. Zhou, D.-D. Zhou, X.-H. Han, and A. Agishev. A kinematic study of the integral shaped filament: what roles do filaments play in forming young stellar clusters? *Research in Astronomy and Astrophysics*, 18:077, July 2018. doi: 10.1088/1674-4527/18/7/77.

K. C. Yu, J. Bally, and D. Devine. Shock-excited H_2 Flows in OMC-2 and OMC-3. *ApJL*, 485: L45–L48, August 1997. doi: 10.1086/310799.

L. A. Zapata, J. Schmid-Burgk, P. T. P. Ho, L. F. Rodríguez, and K. M. Menten. Explosive Disintegration of a Massive Young Stellar System in Orion. *ApJL*, 704:L45–L48, October 2009. doi: 10.1088/0004-637X/704/1/L45.

Hans Zinnecker and Harold W. Yorke. Toward Understanding Massive Star Formation. *ARA&A*, 45(1):481–563, Sep 2007. doi: 10.1146/annurev.astro.44.051905.092549.

Catherine Zucker, Joshua S. Speagle, Edward F. Schlafly, Gregory M. Green, Douglas P. Finkbeiner, Alyssa A. Goodman, and João Alves. A Large Catalog of Accurate Distances to Local Molecular Clouds: The Gaia DR2 Edition. *arXiv e-prints*, art. arXiv:1902.01425, Feb 2019.